MECHANICAL RESPONSE OF POLYMER MATRIX COMPOSITES USING INDENTATION STRESS-STRAIN PROTOCOLS

A Dissertation
Presented to
The Academic Faculty

by

Alicia Marie Glyn Rossi

In Partial Fulfillment
of the Requirements for the Degree
Doctor of Philosophy in the
School of Materials Science and Engineering

Georgia Institute of Technology
December, 2018

MECHANICAL RESPONSE OF POLYMER MATRIX COMPOSITES USING INDENTATION STRESS-STRAIN PROTOCOLS

Approved by:

Dr. Surya Kalidindi, Advisor
School of Mechanical Engineering
Georgia Institute of Technology

Dr. Karl Jacob
School of Materials Science and Engineering
Georgia Institute of Technology

Dr. Kyriaki Kalaitzidou
School of Mechanical Engineering
Georgia Institute of Technology

Dr. Antonia Antoniou
School of Mechanical Engineering
Georgia Institute of Technology

Dr. Hamid Garmestani
School of Materials Science and Engineering
Georgia Institute of Technology

Date Approved: [November 7, 2018]

To my Lord Jesus and to my family, especially my husband Chad.

ACKNOWLEDGEMENTS

I would like to thank my advisor, Surya Kalidindi, for his support and guidance throughout my Ph.D. He has provided invaluable advice, and knowledge which have been critical to my success. I would also like to Dr. Kyriaki Kalaitzidou and Dr. Craig Przybyla for their collaboration and technical expertise which have made these projects possible. I am grateful for the training, guidance, and collaboration of my fellow graduate students in the MINED research group. In particular, I am grateful to Andrew Castillo for his contribution of simulations and David Brough for his collaboration in the structure-property linkage project.

I would like to acknowledge the financial support of the FLAMEL program and of the *ForWarD to Materials Data Science and Informatics (FWD-MDSI)* program provided through the Air Force Research Laboratory.

Finally, I am profoundly grateful to all my friends and family who have been my support and encouragement throughout my graduate program.

TABLE OF CONTENTS

ACKNOWLEDGEMENTS **iv**

LIST OF TABLES **vii**

LIST OF FIGURES **viii**

LIST OF SYMBOLS AND ABBREVIATIONS **xi**

SUMMARY **xiii**

CHAPTER 1. Introduction **1**
1.1 Applications of Polymer Matrix Composites **1**
1.2 Length Scales of Composite Materials **3**
1.3 High-Throughput Testing **5**
1.4 Objectives **6**

CHAPTER 2. Background **8**
2.1 Composite Models **8**
2.2 Testing methods for composite materials **11**
2.2.1 High Throughput Testing 12
2.2.2 Indentation for Interfaces 13
2.2.3 Indentation analysis protocols 15

CHAPTER 3. Spherical IndenTation for the Extraction of Stress-strain Curves **18**
3.1 Hertz Theory **19**
3.2 Application to Load Displacement Data **20**
3.2.1 Effective Initial Contact 22
3.2.2 Indentation Modulus and Contact Area 26
3.2.3 Indentation Stress and Indentation Strain 26

CHAPTER 4. Indentations on Laminate composites **28**
4.1 Introduction **28**
4.2 Materials and Sample Preparation **29**
4.3 Results **33**
4.4 Conclusion **46**

CHAPTER 5. Indentations on Nano-composites **48**
5.1 Introduction **48**
5.2 Materials and Samples **49**
5.3 Surface Preparation **51**
5.4 Steps of Applying the protocols to Nanocomposites **52**
5.5 Results **54**
5.5.1 Raman 54
5.5.2 Indentation Tests 56
5.6 Conclusion **59**

CHAPTER 6. Conclusions and Future Work **60**
6.1 Conclusions **60**
6.2 Future Work **61**

APPENDIX A. Robust Property Structure linkage for polymer composites **63**
A.1 Background **63**
A.2 Methods **64**
A.2.1 Data Generation 65
A.2.2 Workflow 66
A.3 Results and Discussion **73**
A.4 Conclusion **76**

APPENDIX B License **78**
B.1 Rightslink License for the use of Figure 14 **78**

REFERENCES **85**

LIST OF TABLES

Table 1	Measured values of modulus and yield for indentation tests in various angle plies.	40
Table 2	Indentation Modulus and Yield values for tests on PP/CNT samples.	57

LIST OF FIGURES

Figure 1 Hierarchical multi-layer laminates. A) Illustrates the highest lengthscale involving multiple plies. B) Shows the arrangement of multiple fibers within a single ply and C) Shows the scale of the individual fibers and matrix. 4

Figure 2 Optical image of laminate composite overlaid with a grid of testing points for high throughput testing. The variety of local conditions present in a laminate composite make it ideal for high-throughput testing**.** 5

Figure 3 The main steps of the indentation stress-strain analysis protocols. Green colored data points in the initial portion of the machine captured load-displacement data (plot A) are identified to lie in the elastic region of the indentation loading response. This is accomplished from the linear regression performed in Plot B, which in turn identifies the corrections needed to the measured load and displacement signals to bring them in close agreement with Hertz's theory. Plot C shows a regression fit based on Hertz's theory used to determine the effective indentation modulus, which is subsequently used to estimate the contact radius a from the measured CSM. Plot D shows the final extracted indentation stress-strain response. 21

Figure 4 Diagram of the evolution of the area of contact between the indenter and the sample. 24

Figure 5 SEM images showing the height discrepancy between the fiber and matrix. A) Surface after ion polishing showing a large height discrepancy due to different removal rates of the components. B) Surface after 0.05 μm final polish showing decreased height discrepancy. Both images were taken in depth mode to emphasize the contrast in heights. White rings around the fibers indicate the step from the height of the matrix to the fibers. 31

Figure 6 SEM images showing the height discrepancy between the fiber and matrix. A) Surface after ion polishing showing a large height discrepancy due to different removal rates of the components. B) Surface after 0.05 μm final polish showing decreased height discrepancy. Both images were taken in depth mode to emphasize the contrast in heights. White rings around the fibers indicate the step from the height of the matrix to the fibers. 31

Figure 7	AFM data on A) 0, B) 30, and C) 60-degree plies. Each line graph shows the height data for the line drawn on the image above it.	32
Figure 8	Maximum indentation area compared with the size of an individual ply.	33
Figure 9	Example of the results from two different choices of the initial elastic segment. A) Shows the locations of these elastic segments on the raw load-displacement data. B) shows them on the plot which is used to calculate the effective zero-point. C) Shows the stress-strain curves which result from the choice of elastic segment. Also included are grey lines indicating the elastic slope and the offset for determining the yield point. The yield point is indicated in magenta.	37
Figure 10	SEM images showing damage to the material surface after indentation. A) shows an indentation location after test conditions showing matrix cracking. B) shows additional damage to the surface caused by a high-load indentation test. Here extensive debonding can be seen around the fibers.	39
Figure 11	Indentation Stress-Strain curves for indentations in various plies.	40
Figure 12	Comparison of experimental results of modulus with the results of simulations of the indentations.	45
Figure 14	Fracture surface imaged in the SEM clusters of CNTs are shown with the circles and boxes show waviness of the CNTs. Originally published in Bhuiyan et. al.[79] Used with permission.	50
Figure 15	Schematic depicting the dog bone sample from which samples for indentation were cut. The arrow indicates the direction from which the indentations were performed.	51
Figure 16	Steps for the stress-strain analysis of indentation data. A) shows the final stress-strain results. The green points in all the graphs indicate the initial elastic segment chosen for analysis. The red dot indicates the yield point as determined by the 0.2% offset (grey dotted line) B) shows the raw load-displacement data. C) shows the plot used to determine the effective zero-point. D) shows the plot used to calculate the modulus. E) shows the calculated contact radius which is used to determine the stress and strain. For more information on these steps please see chapter 3.	54
Figure 17	Individual Raman results for the 0, 1 and 5 wt% samples. Note the peaks indicating the presence of polypropylene at 808 and 840 cm^{-1}. The peak which most strongly indicates the presence of carbon nanotubes can be found at 1593 cm^{-1}.	55

Figure 18	Indentation tests on 5 weight percent sample.	57
Figure 19	Indentation test results on neat 1wt% and 5wt% PP/CNT samples.	58
Figure 20	One instance from each of the 2D microstructure classes generated for this study. The volume fraction, orientation, and length of the fibers were varied. The aspect ratio of the fibers starting from the left are 20: 1, 5: 1, 1: 20, 1: 5, 1:15, and 15: 1 while the volume fractions for each of the subclasses were around 20%, 30%, 40%, 50%, 60%, and 70% with a ±10% variation.	64
Figure 21	Autocorrelations with fibers for each of the structure shown in Figure 16. The top three autocorrelations correspond to the three structures on the left and the bottom three correspond to the three structures on the right. The tick marks on the x- and y-axes represent the location of the head of a vector with its tail at the origin.	66
Figure 22	The percent variance as a function of principal components computed using Principal Component Analysis (PCA) on the 2-point statistics for each microstructure.	68
Figure 23	Projection of the microstructure space onto the first two principal components (PC). The first PC correlates with the volume fraction of the fibers while the second PC correlations with the orientation and length and orientation of the fibers.	70
Figure 24	Mean and standard deviation of the MSE values found using 3-fold cross-validation as a function of the number of principal components and the degree of the polynomial regression model. The top plot is the log of the mean and standard deviation of the MSE values. The lower plot shows a subset of the parameter space with the best results with mean of the MSE values indicated with the points and the standard deviation is indicated by the shaded region around each point.	72
Figure 25	Goodness of fit plot of effective stiffness values for both training and testing datasets.	73
Figure 26	Goodness of fit plot of showing comparison of the new model with standard models for predicting elastic modulus of composite materials. Rule of Mixtures (ROM) and Haplin-Tsai models were applied to the microstructures and the results compared to the FE results.	74

LIST OF SYMBOLS AND ABBREVIATIONS

PMC	Polymer Matrix Composite
E_1	Modulus in the fiber direction
E_2	Modulus transverse to the fiber direction
E_f	Modulus of the Fibers
V_f	Volume Fraction of the fibers
E_m	Modulus of matrix
V_m	Volume Fraction of matrix
d	Average diameter of fibers
l	Average length of the fibers
P	Load
P_{max}	Maximum load before unloading
E_{eff}	Effective Modulus of the sample indenter system
R_{eff}	Effective radius of contact
h_e	Elastic Displacement
a	Contact Radius
v_i	Poisson's Ratio of the indenter
E_i	Modulus of indenter
v_s	Poisson's Ratio of sample
E_s	Modulus of sample
R_i	Radius of indenter
R_s	The radius of the sample surface
CSM	Continuous Stiffness Measurement

S	Elastic Stiffness from CSM
$\tilde{P}$	Load measured by Indentation Equipment
P^*	Effective point of contact in load
$\tilde{h}_e$	Elastic displacement measured by Indentation Equipment
h^*	Effective point of contact in displacement
σ_{ind}	Indentation Stress
ε_{ind}	Indentation Strain
CF	Carbon Fiber
SEM	Scanning Electron Microscopy
AFM	Atomic Force Microscopy
$\{C_{11}, C_{12}, C_{33}, C_{13}, C_{44}\}$	Elastic Constants
PP	Polypropylene
CNT	Carbon Nanotubes
wt%	Weight Percentage
u	displacement vector field
L	length of the square domain
$\bar{\varepsilon}_{xx}$	average or macroscopic applied strain
MSE	Mean Square Error
E_c	Composite Modulus

SUMMARY

Polymer Matrix Composites (PMCs) are an important material for many advanced applications due to their potential to combine critical mechanical properties with a high strength-to-weight ratio necessary for advancing automotive and aerospace applications. Such materials have been studied extensively for their bulk properties as well as the properties of their individual components. However, there remains an intermediary lengthscale on the order of the arrangement of the reinforcing phase which has yet to be satisfactorily characterized. Understanding the properties of this intermediary lengthscale is critical to the development of multi-scale models with predictive capabilities.

To address this need, the use of instrumented indentation on a lengthscale appropriate to the material system presents itself as a viable solution. Indentation is uniquely suited to such an implementation due to its inherent ability to conform to the lengthscale of testing needed and its high throughput nature. Recent advancement in the data analysis protocols for spherical indentation has allowed for the extraction of stress-strain curves from the load-displacement data resulting from indentation tests in a variety of materials including single and polycrystalline metals, natural materials and polymers. The goal of this thesis is to extend these protocols to address the unique challenges presented by their application to polymer matrix composites.

For this purpose, two disparate materials systems have been chosen to develop the protocols. One is a laminate composite system made from carbon fibers embedded in an epoxy matrix. Here the intrinsic variation within a single ply is tested within the laminate composite. The second material system is a nano-composite composed of multi-walled

carbon nanotubes (CNTs) in a polypropylene matrix. Here the variability in properties due to the presence of agglomerates of the CNTs will be explored. Application to these two different material systems will demonstrate the applicability of these protocols for determining the properties of composites on the desired scale.

CHAPTER 1. INTRODUCTION

At its most basic, a composite is a solid material made up of two or more distinct solid components or phases. To make useful composites, the two primary phases are chosen such that their properties complement each other to make a composite with combined properties. For structural composites, the two main components are typically called the matrix and the reinforcement. The matrix can be a variety of materials such as metal matrix, ceramic matrix or polymer matrix composites. For the purpose of this thesis, the focus will be on polymer matrix composites because of their wide range of applications. The polymer matrix serves to bind the reinforcement together as well as additional properties such as chemical resistance. The reinforcing phase typically enhances the composites mechanical properties such as modulus and yield point. Depending on the application other properties such as thermal or electrical conductivity or resistivity may be contributed by one or the other of the phases. Varying the type and arrangement of the two phases leads to a wide variety of potential composites which can be tailored to the specific needs of various applications.

1.1 Applications of Polymer Matrix Composites

Composites are the most promising lightweight materials suitable for material substitution leading to weight reduction. For the near future, it is expected that today's average 900 kg of steel and other metals can be lowered to 600 kg per car through substitution by composites and hybrid solutions [1]. For example, the all-electric BMW i3 car with an all-composite passenger cell can travel 160 km on a single charge and has significant

manufacturing benefits over cars with metal bodies [2, 3]. In many ways, the drivers for production of lightweight airplanes are similar to those for car manufacturers. Reduced weight leads to decreased fuel consumption and greenhouse emissions. For example, in the aerospace industry, PMCs account for half (by weight) of the primary structure of the new Boeing 787 and are thought to be responsible for the 20-30% reductions obtained in the fuel use and CO_2 emissions when compared to the conventional mostly aluminum aircraft [4-6]. A variety of different fiber and matrix combinations lead to polymer matrix composites to be popular choices for such substitutions. For example, glass, carbon, Kevlar and natural fibers have all been used for automotive applications as the reinforcing material [7]. Matrix materials include a variety of both thermoplastics, such as polypropylene, and thermosets, such as various epoxies, depending on the application requirements. The choice of material combination also depends on other design parameters such as manufacturability, but many combinations provide significant weight savings compared to traditional metals while maintaining the mechanical properties required for their applications.

Composites are also suitable choices for a variety of applications due to the large variety of different types and their adaptability. For example, there are a wide variety of different fiber architecture types. Some of the most common are textile structures (weave, knitted etc.), short fiber composites, long fibers composites and continuous fiber composites which are usually laminate systems. The choice of fiber architecture is often dependent on the expertise and access to equipment of the designer. Structurally, the ability to choose the appropriate architecture for a particular application is very important. The properties of

the final product can be tailored through control of the arrangement of the components of the composite which will be hereafter referred to as the microstructure.

Composites containing a component with at least one dimension on the nano-scale (nano-composites) also present a unique opportunity for tailoring of material properties such as conductivity or chemical resistance or reactivity. Such composites have been used in a wide variety of applications. Often, carbon nanotubes are used in these applications due to the high level of property enhancement which can be achieved with even small ratios of reinforcement to the matrix. In addition, nano-composites have specific advantages in formability and manufacturability if the dispersion of the reinforcing phase can be controlled.

1.2 Length Scales of Composite Materials

An important feature of composites that makes them more able to be tailored to specific applications is the hierarchical nature of these materials. For materials, hierarchy refers to the complexity of the materials at various length scales which contribute to the overall properties of the materials. Composites have details on different length scales which contribute to the overall properties and performance of the material. Figure 1 shows an example of a multi-laminate composite with three primary levels of hierarchy. At the highest level of complexity, the sample is made of many individual lamina with different orientations of the fibers. The second level of complexity is the variation within each of the individual lamina as shown in the central image. This variation includes such variable as local volume fraction and packing factors. The packing of the fibers and the distance

from the center of the lamina create variation within a single ply. The lowest level of complexity is at the level of the individual fibers and the matrix. The third image in Figure 1 shows an individual fiber surrounded by matrix. At this level, the properties of the

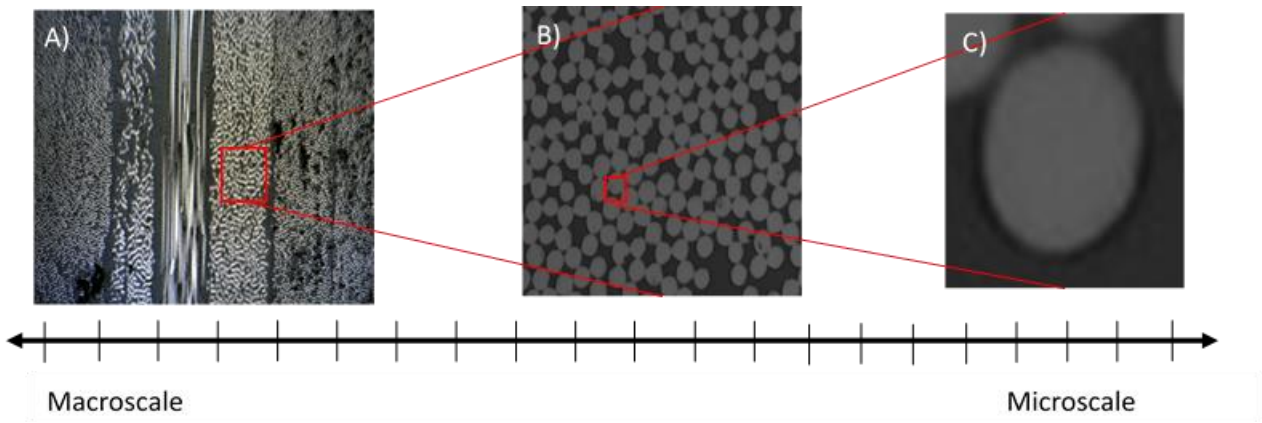

Figure 1: Hierarchical multi-layer laminates. A) Illustrates the highest lengthscale involving multiple plies. B) Shows the arrangement of multiple fibers within a single ply and C) Shows the scale of the individual fibers and matrix.

individual components and the interactions between them affect composite performance. Measures such as adhesion, interfacial strength, and pull-out energy would be measured to characterize the composite at this lengthscale. There are a variety of testing methods for characterizing the first and last lengthscales as will be discussed in the next chapter. However, the intermediate lengthscale requires additional protocols for extraction of the mechanical properties. Typically, this length scale is characterized on average by creating unidirectional plies and using the same testing methods that are used on the macroscale. However, the problem with this approach is that the properties of the ply within the composite are not necessarily the same as those in a unidirectional ply. This discrepancy is usually the result of the local conditions during processing. In addition, there is a high degree of variability in the local structure at this lengthscale. Assuming a single property

for each ply leads to an incomplete understanding of the material hampering efforts to create multi-scale models of these materials. Therefore, the development of protocols for investigating the local variance in properties at this length scale has value for improving such efforts.

1.3 High-Throughput Testing

If we are to be able to characterize the variance in properties at the length scale of interest, it is necessary to be able to perform multiple tests at this lengthscale in a short period of time. By doing so, a variety of local conditions can be examined. Such testing protocols are known as high-throughput testing protocols. An early example of high-throughput testing was demonstrated in the drug discovery industry where tests were developed to test a variety of chemical combinations simultaneously. In order to test mechanical properties in a high-throughput manner, two conditions must be met. The first is that there must be a

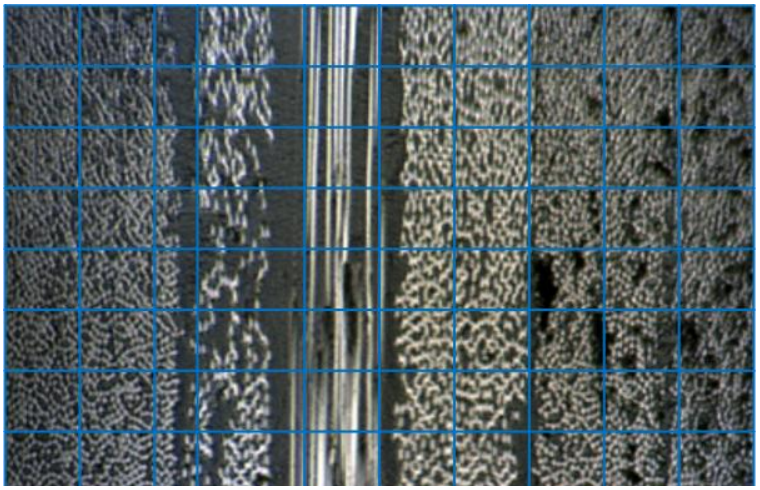

Figure 2: Optical image of laminate composite overlaid with a grid of testing points for high throughput testing. The variety of local conditions present in a laminate composite make it ideal for high-throughput testing.

variety of conditions present in a relatively small volume for testing. For this condition, laminate samples are ideal for testing as each ply will have different conditions and conditions will vary along the length of the ply. Testing can proceed on a grid such as the one shown in Figure 2.

The second requirement for high-throughput testing is a testing method where the tests can be performed and analyzed rapidly. Indentation testing is a good candidate for such a testing method. Many tests can be done in the same sample which decreases the amount of time that it takes to prepare samples. Also, depending on the chosen settings, indentation tests can take approximately 30 seconds to a few minutes for each test to be performed. Dozens of tests can be performed on a single sample very rapidly. The analysis takes a little bit longer than the analysis for bulk methods such as the tensile test, but progress has been made toward automating parts of the process. As a result, the overall time to perform and analyze the test is significantly reduced compared to traditional tests. For this reason, tensile testing can be considered a viable high-throughput option.

1.4 Objectives

The objective of this work will be to develop high throughput testing protocols for use in testing polymer matrix composites at multiple scales with a focus on the length scales corresponding to the arrangement of the reinforcements. This testing method will be intended to the high throughput so as to allow for rapid testing of a variety of potential conditions. High throughput testing will also allow for characterization of the variance in the material. For this objective, I will use spherical indentation test protocols to test the

properties at the local scale. This thesis will investigate the difficulties particular to indentation testing on polymer matrix composites so as to adapt the protocols for use on such materials.

The second objective of this thesis will be to apply the newly developed protocols to two different kinds of PMCs. The first will be a laminate composite such as the one pictured in Figure 1 where layers of fibers embedded with the matrix will be stacked on top of each other at various angles. The second material system will be a nano-composite made with carbon nanotubes. These two material systems were chosen because they are both well-characterized on the macro scale and represent two very different material systems. These applications will serve to validate the protocols that have been developed in this work.

Chapter 2 will give a background of various models and testing methods which have been used to characterize composites in the literature. In addition, it will give some background on methods of determining material properties from the load-displacement data gathered from indentation tests. Chapter 3 will focus on the use of spherical indentation protocols for evaluating the local properties of composites. Chapters 4 and 5 will present the results of applying these protocols to carbon fiber/epoxy laminates and polypropylene/carbon nanotube composites respectively. The final chapter will present concluding remarks and give a vision for future extension of this work.

CHAPTER 2. BACKGROUND

In order to understand the nature of composite materials and how they will react in various use conditions, a combination of models and experiments have been used successfully. Models have limitations in the need for validation and usually limited applicability to a single architecture and/or shape. Experiments, on the other hand, require less validation (although the interpretation of the results may need initial validation) but are usually limited by physical factors such as the shape of the tested sample or the time and material it takes to create and test samples. An ideal system would create models which are then validated by experiments at various lengthscales.

2.1 Composite Models

There are a variety of models that have been used to simulate the mechanics of the composite materials. These models range from simple analytical models to complex finite element simulations. Perhaps the simplest of the analytical models is the Rule of Mixtures. The rule of mixtures defines equations for the calculation of two moduli, the modulus in the fiber direction (E_1) and the modulus transverse to the fiber direction (E_2) [8]. The equation for the first is shown in Eq. 1 and represents the upper bound of possible moduli based on an isostrain assumption. Conversely, the value for the modulus for the transverse direction found in Eq. 2 has been determined to be a lower bound on the possible modulus values when compared with experimental results and is calculated using an isostress approximation. In these equations E refers to the elastic modulus of the material and V to the volume fraction. The f subscripts refer to the fiber properties and the m to the matrix.

$$E_1 = E_f V_f + E_m V_m \tag{1}$$

$$E_2 = \frac{E_f E_{fm}}{V_m E_f + V_f E_m} \tag{2}$$

From these simple bounds, many modifications have been made. One of the most well-known and employed is the Haplin-Tsai equations. These equations are helpful forms of Hill's generalized self-consistent model [8]. This model assumes that the materials are homogeneous and transversely isotropic about the fiber direction. Equations 3 and 4 are formulations of the Haplin-Tsai equations as they pertain to the elastic modulus. These equations can be derived for other material properties (bulk modulus, shear modulus, etc.) but are not considered here. These equations employ the same naming conventions as above with the addition of d corresponding to the diameter of the fibers and l the average length.

$$E_L = \frac{1 + \left(\frac{2l}{d}\right)\eta_l V_f}{1 - \eta_l V_f} E_m \tag{3}$$

$$\eta_l = \frac{\frac{E_f}{E_m} - 1}{\frac{E_f}{E_m} + \frac{2l}{d}} \tag{4}$$

In addition to these models, there are other analytical models that have been developed to predict mechanical properties of fiber composites such as models based off of shear-lag

theory[9] and variations thereof[10]. However, all of these approaches are designed for short fiber composites with specific volume fractions and cannot be used accurately for systems outside of this range.

Laminate type composites have their own set of methods for predicting the properties of the composite. The most commonly used analytical method is Classical Lamination Theory[11]. Some of the models are applicable to multiple types of textiles but most are restricted to a specific material geometry.

Many finite element models have also been constructed to determine the properties of various fiber architectures. Such models have been designed to determine a variety of material properties including elastic modulus[12-14], thermal conductivity [12, 13] delamination[15], failure [16, 17] and interphase properties[18]. Most of these models have been designed from random perturbations of the structure from microstructural features such as volume fraction and fiber length distribution. However, some of these constructs have been designed based on the actual microstructure. One method of doing this is to mesh the structure according to the voxels such that each voxel becomes an element in the mesh and the corners are nodes. However, this method has the drawbacks of creating a large number of elements and potentially jagged interfaces. Instead, some researchers have developed means of using the microstructure images as source data for creating a mesh that approximates the microstructure[19]. This approach combines pixels in non-critical areas to decrease the mesh size and smooths the interfaces between the components of the microstructure. These approaches have proven effective in glass fiber composites[20].

What many of these models have in common is some level of homogenization is assumed. Usually, this homogenization occurs at the level of the organization of the individual fibers. For example, many of the above-mentioned models assume that the fibers are evenly spaced on a grid. However, depending on the processing methods and conditions there can be a large amount of heterogeneity at this lengthscale. As a specific example, there often is a significant variation in the local mechanical properties between the regions near the center and near the edge of the plies (i.e., single laminates), attributable to the differences in the fiber packing density as well as the geometry and chemical compositions of the interphase regions. This variance is often a natural consequence of the details of the processing conditions employed in the manufacture of the multi-laminate composite systems. New test protocols that can quantify the variance in local mechanical properties at the scale of multiple individual fibers within a single laminate can not only provide new insights into the overall composite response but also provide critically needed guidance for fine-tuning the manufacturing conditions leading to improved performance of the manufactured final product. Such testing protocols could also be used on a variety of other types of polymer matrix composites to give insight into the local properties even when the local structure is not easily measured under the conditions in the product. For example, oftentimes the arrangement of components in a nano-composite can only be seen at a fracture surface. Testing protocols to determine the properties at a local scale could offer insight into the variation at the local scale in these materials.

2.2 Testing methods for composite materials

Most of the currently explored models for effective properties of multi-laminate systems employ homogenization at two levels of hierarchy in the material structure – one at the level of a single laminate (i.e., individual fibers in more or less a single orientation embedded in a matrix) and the other at the level of multiple laminates [21-24]. Such modeling efforts critically need appropriate experimental measurements for validation as well as refinement. Indeed, there currently exist a number of well-established test protocols for measuring properties at the level of individual fibers (e.g., tensile tests on fibers [25], fiber pullout [26]) and at the macroscale (e.g., tension tests [27], compression [28], bending tests [29], interlamellar fracture tests [30]). Some of these tests such as tensile and compression can apply to a wide variety of composite systems while some are such as interlamellar fracture tests are specific to a type of composite, in this case, laminar composites. However, there currently exists a large gap in testing protocols between the macro level and the level of individual components. This is the level of collections of components such as a single laminate in a multi-laminate system. More specifically there is a critical need to understand the inherent variance in the local mechanical properties at the level of multiple individual fibers in a single laminate of a multi-laminate system. In other composites, this gap exists as well such as the agglomeration of nano-reinforcement in a nano-composite.

2.2.1 High Throughput Testing

From a practical viewpoint, it is also important to seek high throughput test protocols for measuring the variance in the local properties as one should anticipate the need to conduct a large number of tests within each ply of a multi-laminate system in order to establish the

results with acceptable statistical significance. High throughput techniques also have the potential to be used to map the variance in properties in the nano-composites. Indentation techniques have been widely used in prior literature for establishing the local properties at a different location in a manufactured final product [31, 32]. Instrumented indentation is a test method to probe the mechanical properties of a material by pressing into the material with a tip of a specified geometry and measuring the load and displacement response. From the response, the material properties can be determined. Indentation testing offers many advantages in characterizing the mechanical response of materials at different material length/structure scales. Various forms of indentation testing have been used to explore the properties of composites in literature.

2.2.2 Indentation for Interfaces

One significant use of indentation techniques in polymer matrix composites is to examine the interfaces between the reinforcement and the matrix. This is done in two primary ways at different lengthscales. The first is to use an indenter to push on individual fibers and using the response to measure the interface shear strength. Several researchers including Desaeger and Verpoest [33] have used indentation techniques in this way. Indentations were performed in the center of fibers embedded in the matrix. This had the advantage of being able to test fibers with the confinement caused by other fibers surrounding it, unlike fiber pullout tests. Indentations were performed on the fibers and optical processing was used to determine if debonding had occurred. Then they determined the debonding load which was defined as the load at which a debonding crack had a 50% chance of occurring. Then the shear lag method was used to approximate the interface shear strength from this

debonding load. There was no indication in the load-displacement data to show that debonding had occurred. This observation suggests the need for protocols which can transform the load-displacement curve into a stress-strain curve. Recognizing the need to identify the debonding in the mechanical data (as opposed to the image data) Kharrat et.al. [34] attempted to separate the influence of the compression by the matrix from the elastic-plastic response in the load-displacement data. As a result, they were able to determine the debonding load without the need to perform multiple tests at varying loads. This determination was important as it allowed them to determine the debonding load more precisely using less experimental tests. However, both of these efforts were hampered by the use of sharp indenters which often caused fiber splitting.

In addition to interface properties indentation has also been used to determine the properties of the region of matrix closest to the reinforcement which is known as the interphase. This region has been shown to have properties different from the bulk of the matrix due to chemical and physical interactions between the reinforcement and matrix.[35] Testing of this region is done by a series of tests at a very small lengthscale in order to look at the variation in properties across the interface. Hodzic and collaborators[36-39] used such techniques to investigate the effects of environmental conditions on the size and properties of the interface in various materials. These tests showed a clear difference in mechanical modulus and hardness in the region closest to the reinforcing phase. Other researchers have also shown the existence and extent of the interphase through similar indentation tests[40-42].

However, most indentation protocols employed in current literature evaluate the material's modulus and hardness from the unloading segments [43]. Although hardness serves as a surrogate measure of the material's resistance to plastic deformation, it does not have a precise quantitative connection to the elastic-plastic constitutive response exhibited by a material. Hardness is imprecise because it corresponds to the yield strength in the material after a finite but nonstandard amount of plastic deformation that depends both on the material being tested as well as the indenter tip geometry. Recognizing this challenge, there have been several attempts in literature aimed at recovering stress-strain curves from the load-displacement measurements obtained from indentation [44-49].

2.2.3 Indentation analysis protocols

The most popular method of analyzing indentation tests is known as the Oliver-Pharr method. This method can be adjusted for a variety of indenter shapes but is most commonly employed with a sharp indenter such as a Vickers tip or a Berkovich one. [31] This method uses the maximum load of the test and the slope of the unloading curve in order to calculate the hardness and the modulus of the material according to Eqs. 5 and 6.

$$H = \frac{P_{max}}{A} \tag{5}$$

$$S = \frac{2}{\sqrt{\pi}} E_{eff} \sqrt{A} \tag{6}$$

Both of these measurements require the use of an area function (A) which is usually calibrated using an indentation tests on standard material. However, this method requires the use of a standard material which is similar to the material which is desired to be tested in order for the area function to be effective. The other variable used in these equations are marked on the load displacement curve shown in Figure 3. In addition, the calculation of properties based on the unloading curve means that the properties are calculated based on the damaged material. One reason for the use of the unloading portion is that indentation with a sharp tip initiates plasticity in the very early segment of the test. The portion of the curve with only elastic deformation is very small as indicated by the box in Figure 3. Therefore, the initial elastic region cannot be used to calculate the properties of the material using a sharp indenter. To address these issues, spherical indentation protocols have been developed.

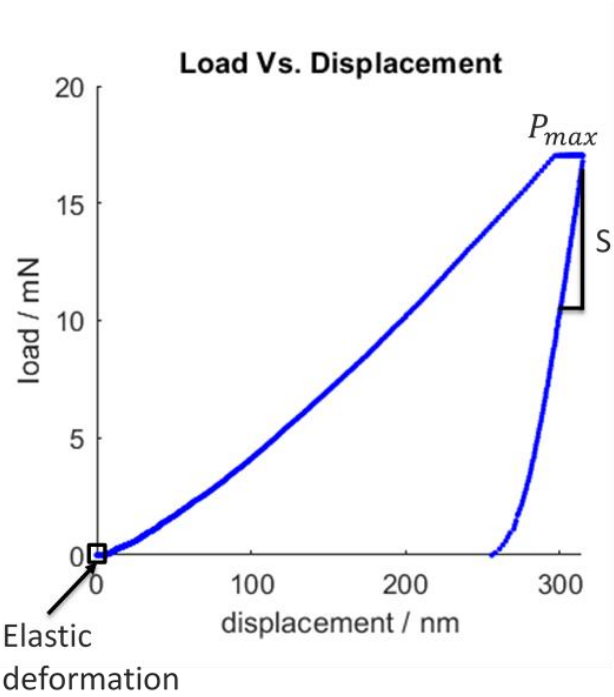

Figure 3*: Load Displacement curve for analysis by Oliver-Pharr Method. Using a sharp indenter, the elastic deformation would in a small initial section as captured in the box. The stiffness at the end of the test, labeled by S, and the maximum load, P_{max}, are also used for the analysis.*

The protocols developed by Kalidindi's research group [49] have demonstrated tremendous promise in terms of the interpretability of the extracted stress-strain curves [50, 51] at multiple length scales (of the indented volumes in the samples) [52], and their broad applicability to many different materials systems [52-60]. These protocols will be discussed in detail in the next chapter.

CHAPTER 3. SPHERICAL INDENTATION FOR THE EXTRACTION OF STRESS-STRAIN CURVES

Instrumented indentation is a test method to probe the mechanical properties of a material by pressing into the material with a tip of a specified geometry and measuring the load and displacement response. From the response, the material properties can be determined. Indentation testing offers many advantages in characterizing the mechanical response of materials at different material length/structure scales. However, most indentation protocols employed in current literature evaluate the material's modulus and hardness from the unloading segments [43]. Although hardness serves as a surrogate measure of the material's resistance to plastic deformation, it does not have a precise quantitative connection to the elastic-plastic constitutive response exhibited by a material. Hardness is imprecise because it corresponds to the yield strength in the material after a finite but nonstandard amount of plastic deformation that depends both on the material being tested as well as the indenter tip geometry. Recognizing this challenge, there have been several attempts in literature aimed at recovering stress-strain curves from the load-displacement measurements obtained from indentation [44-49]. The protocols developed by Kalidindi's research group [49] have demonstrated tremendous promise in terms of the interpretability of the extracted stress-strain curves [50, 51] at multiple length scales (of the indented volumes in the samples) [52], and their broad applicability to many different materials systems [52-60]. These protocols are based on the relationships established by Hertz

(citation) for the elastic, frictionless, contact between two isotropic, homogenous, bodies exhibiting quadratic surfaces.

3.1 Hertz Theory

The analysis of the load-displacement data produced by the frictionless elastic contact of a spherical indenter with a flat surface is accomplished by Hertz [61] theory expressed as:

$$P = \frac{4}{3} E_{eff} R_{eff}^{1/2} h_e^{3/2} \tag{7}$$

$$a = \sqrt{R_{eff} h_e} \tag{8}$$

$$\frac{1}{E_{eff}} = \frac{1 - v_i^2}{E_i} + \frac{1 - v_s^2}{E_s} \tag{9}$$

$$\frac{1}{R_{eff}} = \frac{1}{R_i} + \frac{1}{R_s} \tag{10}$$

In these equations P and h_e are the indentation load and the elastic indentation displacement, respectively. They are related by the effective modulus (E_{eff}) and the effective radius of contact (R_{eff}) as shown in Eq. 5. These quantities are related to the individual properties of the indenter and the sample through Eqs. 7 and 8, where E_i, v_i, and R_i denote the modulus, Poisson's ratio and radius of the indenter, and the corresponding variables with the *s* subscript are the variables corresponding to the sample being indented. Equation 6 provides a relationship for determining the contact radius a (corresponding to

the edge of the contact between the indenter and the sample surfaces) under load. However, the availability of continuous stiffness measurement (i.e., CSM) option on modern indenters allows an independent estimation of a at every point in the measured load-displacement curve using the following relation that can be derived from Hertz's theory:

$$a = S/2(E_{eff}) \tag{11}$$

where $S = dP/dh_e$ denotes the measured elastic stiffness.

3.2 Application to Load Displacement Data

There are three main steps to using these equations for extracting the indentation stress-strain responses of the sample material.

1. Determination of the effective zero-point of contact between the indenter and the surface.
2. Calculation of effective modulus and estimation of the contact radius at every point in the load-displacement curve.
3. Computation of indentation stress and indentation strain values.

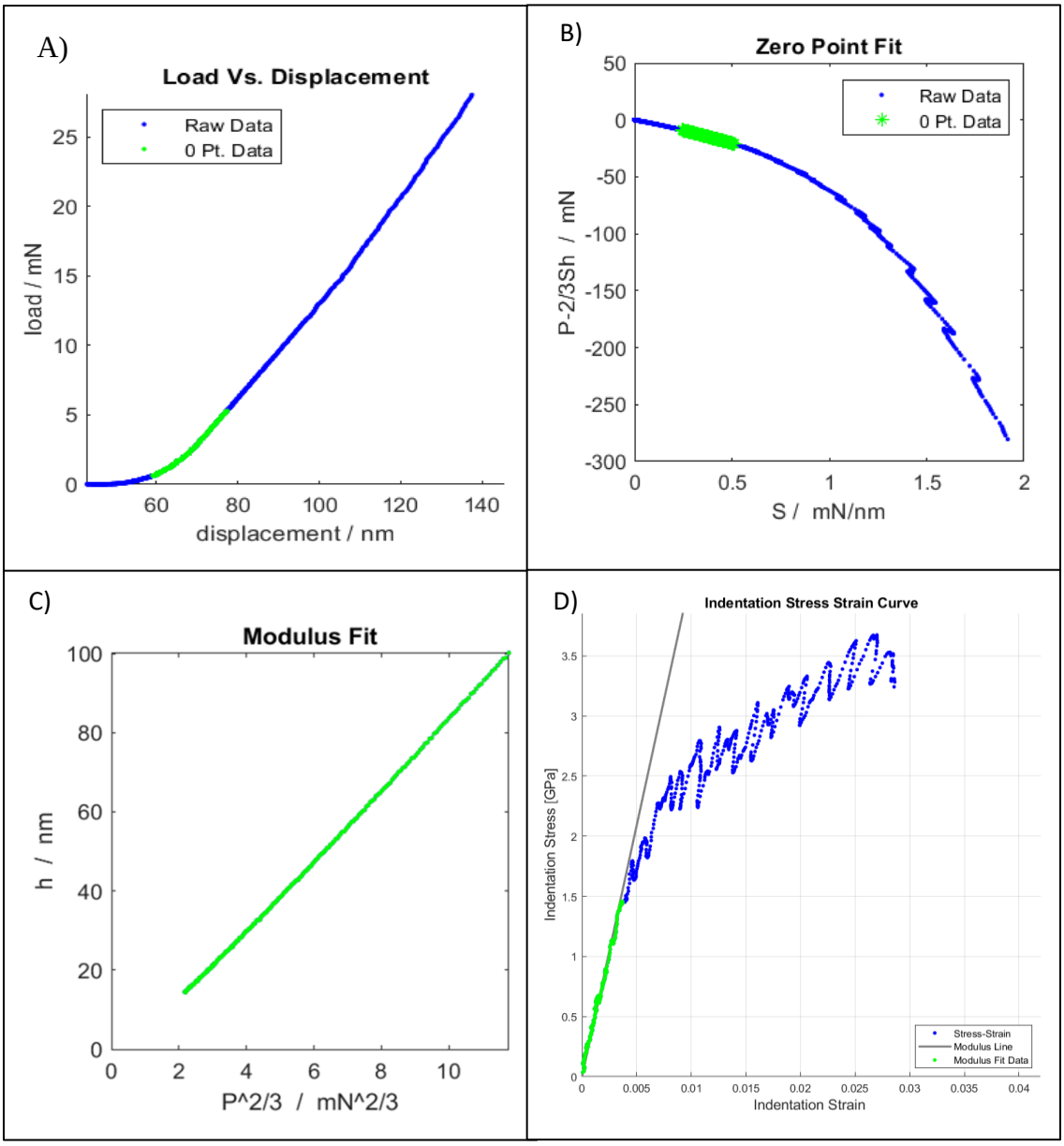

Figure 4: The main steps of the indentation stress-strain analysis protocols. Green colored data points in the initial portion of the machine captured load-displacement data (plot A) are identified to lie in the elastic region of the indentation loading response. This is accomplished from the linear regression performed in Plot B, which in turn identifies the corrections needed to the measured load and displacement signals to bring them in close agreement with Hertz's theory. Plot C shows a regression fit based on Hertz's theory used to determine the effective indentation modulus, which is subsequently used to estimate the

contact radius a from the measured CSM. Plot D shows the final extracted indentation stress-strain response.

3.2.1 Effective Initial Contact

There are many unavoidable factors that contribute to an imperfect (far from ideal) contact between the indenter and the sample. These include roughness of the surfaces, friction, and deviations from idealized geometries of the indenter and sample surfaces. Consequently, one needs to adopt a point of effective contact [49, 62]between the surface and the indenter in the analyses of the raw data obtained from the indentation experiments. The vendor-provided software available in most indenters identifies this contact point by an analysis of the measured CSM values; but it has been shown that this approach results in erroneous extraction of the indentation stress-strain responses [49, 63]. Instead, this is accomplished in this work by determining the relationship expected between the measured values of the load, displacement, and stiffness to be in conformance with Hertz theory (based on Eqs. 5 and 9), and is expressed as:

$$S = \frac{3P}{2h_e} = \frac{3\,(\tilde{P} - P^*)}{2(\tilde{h}_e - h^*)} \tag{12}$$

The tilde on top of a variable indicates that the value is the one measured by the machine, while the star indicates its zero-point correction. A regression analysis of the measurement data within the elastic region (see Plot B, Figure 4) to Eq. 10 can be used to determine these values accurately. The selection of the initial elastic segment for this regression analyses

(the green colored segment in Plot A, Figure 4) is critical to determining the zero-point and has a tremendous effect on the extracted indentation stress-strain curve.

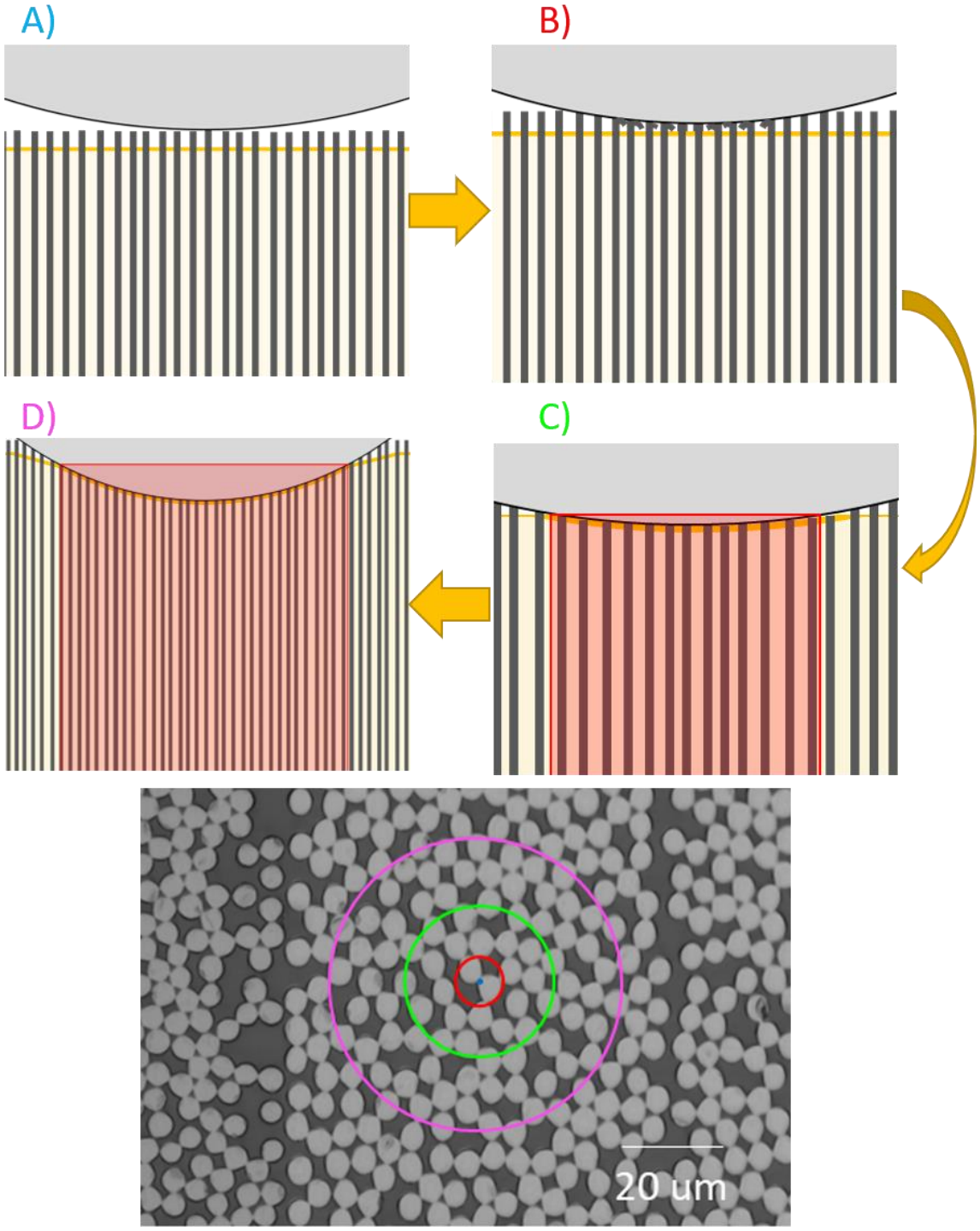

Figure 5: Diagram of the evolution of the area of contact between the indenter and the sample. A) Initial point contact where the indenter and fibers are in contact. B) Incomplete contact between the indenter and material. Area of contact is indicated on the optical

image at the bottom by the red circle. C) The indenter is in contact with both fiber and matrix and a representative volume is being influenced by the indenter. The surface area of contact is represented by the green circle in the optical image. D) Indenter influence by the end of the test. Contact area indicated by the magenta circle is significant but entirely within a single ply.

A significant challenge is encountered in the analyses of the measured raw data from the PMC samples studied in this work. The inherent heterogeneity in the sample results in large changes in the material content of the deformation zone under the indenter, which is especially marked during the initial contact. As the contact zone size changes, the fiber content and the effective elastic stiffness in the primary indentation zone (i.e., the most stressed region in the sample under the indenter) also change dramatically. The changes in the effective elastic stiffness are exacerbated by the very high contrast in the mechanical properties of the constituents (i.e., fiber and matrix). Figure 5 shows four stages of the evolving contact; initial contact indicated in blue and in part A, contact with multiple fibers and the matrix indicated in green and contact at the conclusion of the test indicated in yellow. Since the analysis's procedure depends heavily on Hertz's theory and assumes a constant value of the indentation modulus in recovering the indentation stress-strain curves, one should expect to encounter difficulties in identifying and recovering the initial linear elastic portion of this curve. Of course, once a substantial amount of contact has been established between the indenter and the sample (i.e., the primary indentation zone includes multiple individual fibers), one can expect the effective elastic stiffness in the indentation zone to asymptote to its effective value for the composite. It should also be pointed out that the degree of elastic anisotropy exhibited by PMC plies is significantly larger than what was encountered in all previous applications of the spherical indentation stress-strain

protocols. A finite element model of the indentation test will be compared with the experimental results to validate the applicability of this Hertz based process to these anisotropic materials.

3.2.2 Indentation Modulus and Contact Area

Once the initial contact point has been determined, the corrected data can be used to determine effective modulus and the radius of contact between the indenter and the surface. As seen in Eq. 9, a is related to the stiffness and the effective modulus. E_{eff} can be determined from a regression analysis of the zero-point corrected data using Eq. 5 on the initial elastic loading segment (the green colored segement in Plot C, Figure 4). With the use of the CSM, stiffness is directly measured at every point on the load-displacement data. Then a can be calculated as shown in equation 5.

3.2.3 Indentation Stress and Indentation Strain

In order to transform the measured load-displacement data into meaningful indentation stress-strain curves, one needs to develop and adopt suitable measures of indentation stress and indentation strain. These are meant to represent effective volume-averaged quantities in the primary deformation zones underneath the indenter. However, because of the difficulties involved in solving for the stress and strain fields in the indented region during elastic-plastic indentations, it has not been easy to establish these definitions. Furthermore, the lack of a clear definition of the size of the deformation zone is a major impediment in the development of these concepts. Recent work has suggested the use of the following definitions of the indentation stress, σ_{ind}, and the indentation strain, ε_{ind} [49, 50, 64]:

$$\sigma_{ind} = \frac{P}{\pi a^2} \tag{13}$$

$$\varepsilon_{ind} = \frac{4}{3\pi}\frac{h}{a} \tag{14}$$

Since the values for all of the variables in these equations have already been established in the protocols described earlier, it is relatively easy to extract the indentation stress-strain curve (PlotD, Figure 4). From the extracted indentation stress-strain curve, intrinsic properties of the material such as the indentation modulus and the indentation yield strength can be determined. In this work, we will estimate the indentation modulus from the slope of the initial portion of the indentation stress-strain curve. The indentation yield point will be determined from the intersection of the indentation stress-strain curve and a 0.2% indentation plastic strain offset line exhibiting the slope of the indentation modulus. The stress-strain curve in this intersection region will be smoothed to produce a robust estimate of the indentation yield strength for the composite. Thus far there are no examples in the literature where these protocols have been applied to polymer matrix composites. The following chapters will show that application of these protocols to two different composite systems. The results from the use of these protocols on laminate composites will be discussed in chapter 4 and their application to a nano-composite will be discussed in chapter 5.

CHAPTER 4. INDENTATIONS ON LAMINATE COMPOSITES

4.1 Introduction

The ability to quantify the variance in the local mechanical properties in individual plies is critically important to improve and validate multiscale models. Oftentimes, the properties at the level of the individual plies are determined by creating unidirectional samples and testing them in standard test protocols. However, it has been shown that the properties of the individual plies within a multi-laminate system may not be the same as those measured in the unidirectional samples specifically produced for this purpose [65-67]. In large part, this is due to the differences in the processing conditions experienced by the plies in the two samples (i.e., a multi-laminate sample and a single laminate sample). Therefore, a method for directly measuring the local mechanical properties in the individual plies of a multi-laminate system along with their associated variance is critically needed.

From a practical viewpoint, it is also important to seek high throughput test protocols for measuring the variance in the local properties as one should anticipate the need to conduct a large number of tests within each ply of a multi-laminate system in order to establish the results with acceptable statistical significance. Indentation techniques have been widely used in prior literature for establishing the local properties at different locations in a manufactured final product [32, 68, 69]. Recent advances in indentation instrumentation have tremendously improved the measurement resolution limits, and have now made it possible to measure local properties at exceedingly small length scales [31, 70]. More recently, advances have also been reported in the analyses of the load-displacement data

measured in spherical indentation tests that result in a suitably normalized material response in the form of indentation stress-strain curves [57, 62, 71]. These spherical indentation stress-strain curves exhibit a clear elastic regime and a clear transition to elastic-plastic regime allowing one to reliably establish intrinsic material properties. Furthermore, the material properties measured in the spherical indentation stress-strain protocols can be correlated to the material properties measured in standard tension/compression tests for selected materials classes [50, 51, 64]. The new spherical indentation stress-strain protocols mentioned above have thus far been demonstrated on single and polycrystal properties in metals [55, 72], carbon nanotube brushes [60], bone [73, 74], and visco-elastic properties in polymers [75].

The main goal of this work is to extend the application of the recently developed spherical indentation stress-strain protocols to evaluating the local mechanical response and its variance in the individual plies of a multi-laminate PMC (polymer matrix composite). This extension has encountered several hurdles in both the sample preparation and the extraction of the indentation stress-strain responses from the raw load-displacement data. All of these hurdles mainly arise because of the high levels of heterogeneity between the individual properties of the matrix and the fibers constituents as well as the anisotropy in the mechanical response of the fibers. This paper describes these extensions in detail and reports the indentation stress-strain responses measured in individual plies of a multi-laminate PMC sample.

4.2 Materials and Sample Preparation

Samples for the current indentation study were cut from specimens produced for testing in a technical research program conducted by the Air Force Research Laboratories (AFRL) designed to evaluate various composite damage models [9, 10, 46, 47]. These samples were selected for our study as their macroscale properties had already been systematically evaluated. The samples were made from IM7/977-3 Carbon Fiber/Epoxy. Plates of carbon fiber impregnated with epoxy were layered into a $[30/60/90/-60/-30]_{2S}$ laminate composite. One sample was cut such that the fibers were at 0, 30, and 60 degree angles to the indentation direction. A second sample was cut such that fibers made 30, 60 and 90-degree inclinations to the indentation direction. Both samples were mounted in epoxy mounts and were initially polished using standard protocols[38].

PMC sample preparation for the indentation experiments proved to be a significant challenge for extracting reliable indentation stress-strain curves. The large differences in the mechanical properties of the polymer matrix and the fiber made it very difficult to obtain the flat surface needed for the indentation test while ensuring only a minimal (ideally zero thickness) top disturbed layer (a consequence of cutting the sample and mechanically polishing the sample surface). In general, most mechanical polishing methods or ion-milling methods used to remove the top disturbed layer will result in selective removal of the softer phase compared to the harder phase, creating unacceptable height differences between the matrix and the fiber. Therefore, polishing techniques must be adapted to minimize these height differences.

A Struers Tegramin 30 automatic polishing machine was used to perform the mechanical polishing. Following earlier protocols established in our research group [38],

grinding papers of 1000 grit, 2400 grit, and 4000 grit were used in turn for approximately 2 minutes each. Samples at the end of each polishing step were evaluated by an optical microscope to ensure that damage from the previous polishing step was removed before proceeding to the next polishing step. After all the grinding steps were completed, the samples were polished with a diamond suspension, first with 3 μm particles, and then with 1 μm particles. Each of these steps lasted approximately 15 minutes or until it was determined that the damage from the previous step had been removed. Next, a colloidal silica suspension was used as a final step for 20 minutes. At this point, all apparent damage to the surface was removed. However, it was determined that the addition of another step using a 0.05 μm polishing suspension for another 20 minutes decreased discrepancy in height between the fiber and the matrix as seen in the SEM (scanning electron microscope) images shown in Figure 6.

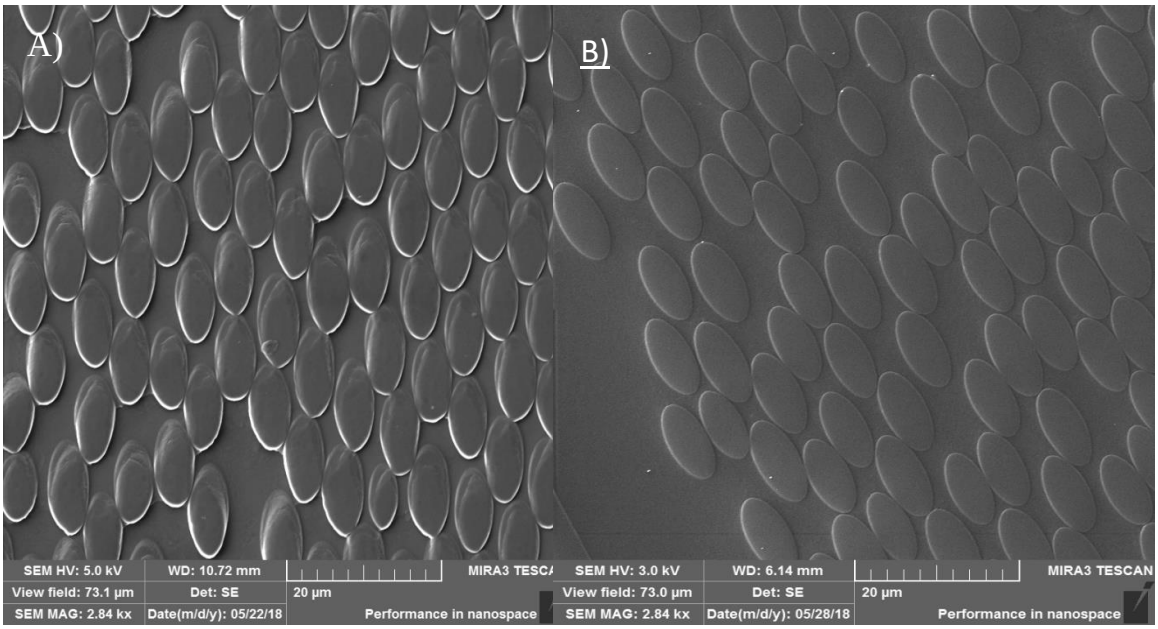

Figure 6: SEM images showing the height discrepancy between the fiber and matrix. A) Surface after ion polishing showing a large height discrepancy due to different removal rates of the components. B) Surface after 0.05 μm final polish showing decreased height

discrepancy. Both images were taken in depth mode to emphasize the contrast in heights. White rings around the fibers indicate the step from the height of the matrix to the fibers.

The final polish was examined by SEM and the height discrepancy was determined to be less than 1 μm as both the fibers and matrix were in focus with a focal depth of this height. Atomic Force Microscopy(AFM) was employed to quantitatively determine the height difference between the matrix and the fibers more precisely. Figure 7 shows an

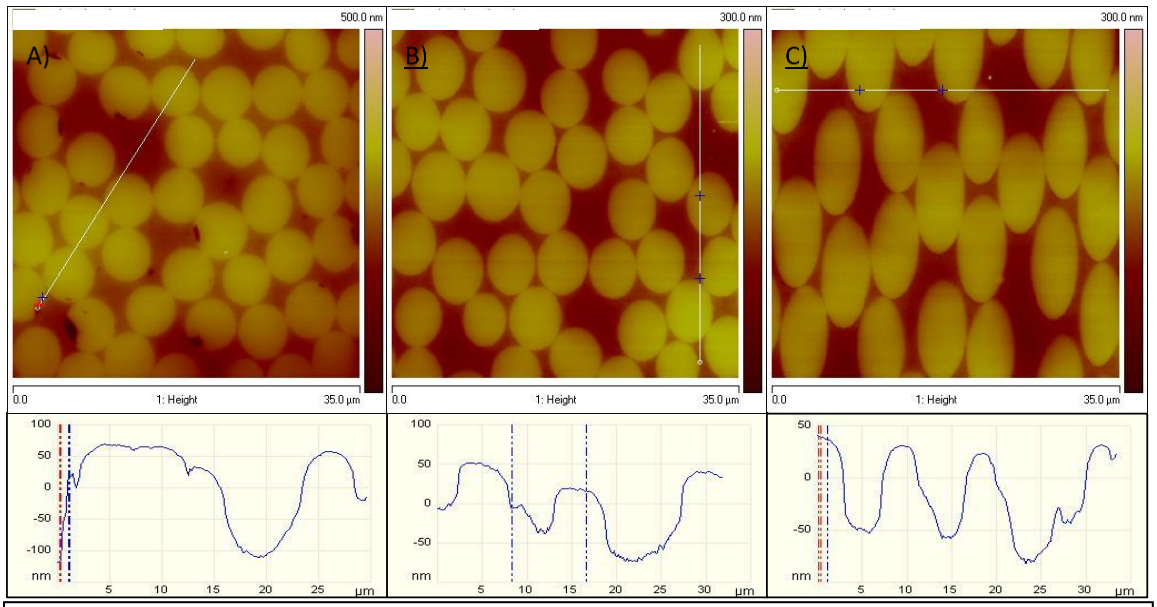

Figure 7: AFM data on A) 0, B) 30, and C) 60-degree plies. Each line graph shows the height data for the line drawn on the image above it.

example of the AFM image generated for one of our PMC samples prepared used the protocols described above. From this data, it was determined that the maximum height difference between the matrix and fiber is approximately 100-150 nm. This value is low enough so as to allow the indenter to come into contact with both the fibers and the matrix before the material exhibits plastic deformation. It should be noted that the height difference varies somewhat depending on the packing of the fibers. The matrix which falls

in between closely packed fibers exhibited a smaller height difference compared to the matrix between more loosely packed fibers.

Indentation tests were performed using an Agilent G200 nanoindentation setup equipped with continuous stiffness measurement (CSM) capability. A tip of radius 500 μm was used as it produced a contact radius of about 25-30 μm at indentation yield. As the plies used in this study were approximately 100 μm wide, and all the indentations were performed along a line near the centerline of the ply (in the thickness direction), all of the indentation deformed zones in the tests reported in this work were confined to lie well within the tested plies (i.e., there is no effect from the ply edges). Tests were run to a maximum load of 700 mN at a target strain rate of 0.05 s^{-1} and then unloaded at the same

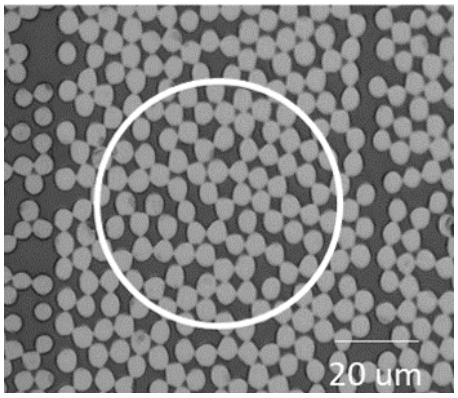

Figure 8: Maximum indentation area compared with the size of an individual ply.

rate. The CSM option was used at a frequency of 45 Hz and an amplitude of 2 nm as recommended by Vachhani et al. [41].

4.3 Results

In the indentation test, it is important to ensure that a good contact has been established between the indenter and the surface to ensure that the measured response comes from the

composite, and not just from the fibers sticking out of the sample surface (see Fig. 5A from Chapter 3). The dramatic increase in the size of the deformation zone under the indenter in the early portions of the indentation test poses a significant challenge in the extraction of reliable indentation stress-strain curves from the PMC samples studied in this work. As one might expect, in the early portion of the load-displacement curve, the fiber volume fraction in the indentation zone will change in an unpredictable manner with the increase in indentation depth (or load). The contact of the indenter with the surface during this region is illustrated in Figure 5B and indicated by the innermost circle on the micrograph in Figure 5. Only after reaching a reasonable deformation zone size (see Figure 5C), one might be able to treat the material in the deformation zone as a homogenized material with the effective properties of a single laminate. Therefore, only the load-displacement data beyond the point of substantial contact (see Figure 5C) can be analyzed with the Hertz's theory introduced earlier. The deformation zone size corresponding to the onset of indentation yield is shown in Figure 5D.

It should be noted that there was always some material heterogeneity even in the metal samples tested in prior work using the spherical indentation stress-strain protocols described above. In the metal samples, this heterogeneity usually comes from a variety of defect distributions in the deformation zone that might include dislocation networks and precipitates. However, since the deformation zone sizes become significantly larger than the length scales associated with these defects at very low indentation depths (or loads), we often only need to ignore only the very early portions of the measured load-displacement curves. In the PMC samples studied here, it was found that we had to ignore

a much larger portion of the measured initial load-displacement data because of the following reasons: (i) the length scale of heterogeneity (i.e., fiber diameters) in the deformed zone of the indentation is significantly larger; and (ii) the contrast in the mechanical properties of the constituents is much larger (i.e., the fiber elastic stiffness is orders of magnitude larger than that of the matrix) leading to large swings in the effective stiffness of the material in the deformation zone in the early stages of the loading.

Recognizing and understanding the challenges described above, it becomes clear that one needs a completely new strategy for selecting the initial elastic segment in the measured load-displacement data for the proper extraction of the indentation stress-strain curves in PMC samples. It should be remembered that this selection influences strongly the identification of the effective zero-point, which in turn affects the computation of all values of the indentation stresses and the indentation strains. Figure 9 illustrates the effects of the selection of two different choices of the initial elastic regimes for the analysis of the same measurement dataset which resulted from a test in a 60-degree ply. The red-colored segment in Figures 9A and 9B indicate a choice of the elastic segment from an early portion of the measured load-displacement data, closer to what one might have selected using the protocols employed currently in the analyses of indentation data acquired in metal samples. However, for the PMC samples, this data comes from a regime where the indenter is not fully in contact with the composite as illustrated in Figure 9B. Recall that the height differences between the matrix and fibers could be as large as 50-150 nm as shown in Figure 7. For the reasons explained earlier, we need to eliminate the measured data in PMC samples at the lower indentation displacement levels from the indentation stress-strain

analyses. This naturally leads to the identification of the green-colored segments in Figures 9A and 9B as our initial elastic segment for the PMC samples. Figure 9C shows the extracted indentation stress-strain curves resulting from the different selections of the initial elastic segments from the same measured load-displacement data. It is seen that the incorrect selection of the initial elastic segment (colored red) leads to an indentation stress-strain curve with multiple unnatural artifacts such a nonlinear elastic regime (at the low stress or strain levels) and an artificial drop in the indentation yield stress (just below an indentation stress of about 0.2 GPa). The correct selection of the initial elastic segment (colored green) produces a much more accurate representation of the indentation stress-strain response in the PMC samples. In later sections, we will further validate the indentation moduli extracted from the protocols described above using finite element simulations. For now, it is emphasized that a simple rule to avoid selecting the early portions of the load-displacement curves for elastic analyses is to discard any selection that produces ann h* (zero-point correction for displacement) value less than the height difference between the fiber and matrix on the sample surface.

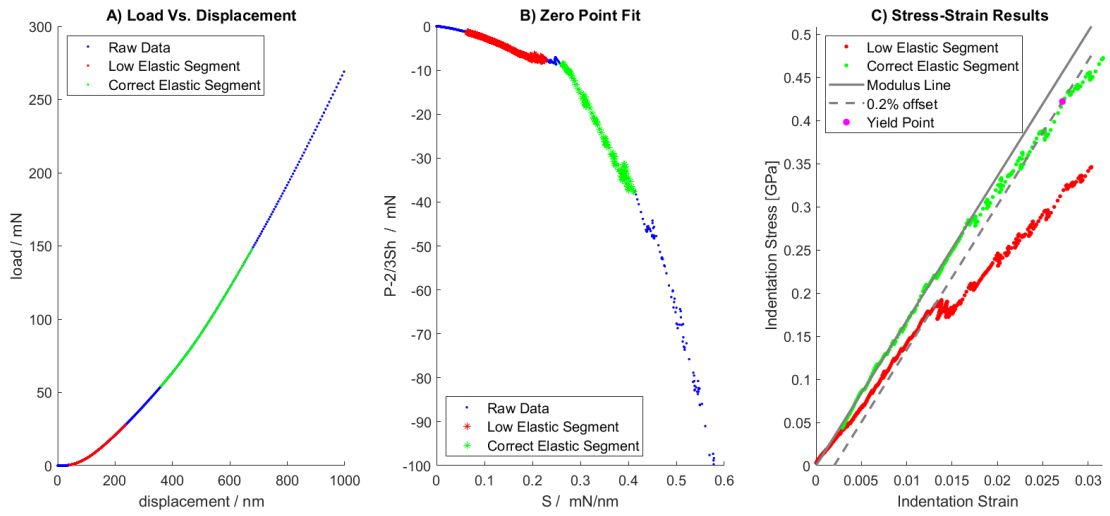

Figure 9: Example of the results from two different choices of the initial *elastic segment. A) Shows the locations of these elastic segments on the raw* load-displacement *data. B) shows them on the plot which is used to calculate the effective zero-point. C) Shows the stress-strain curves which* result *from the choice of elastic segment. Also included are grey lines indicating the elastic slope and the offset for determining the yield point. The y*ield *point is indicated in magenta.*

The green colored indentation stress-strain curve in Fig. 6C (measured in a ply with fibers at 60 degrees to the indentation direction) clearly shows a linear elastic portion. This confirms that a linear relationship continues to exist between P and $h_e^{3/2}$ (implied in Hertz's theory; see Eq. (1)) even for the highly anisotropic case of PMC laminates. To the best of our knowledge, this has never been confirmed in either prior experiments or finite element simulations. The central implication from this important observation is that it would be possible to apply Hertz's theory to materials exhibiting a highly anisotropic elastic response, where E_{eff} could be interpreted as an equivalent isotropic indentation modulus of the sample material. Of course, additional work would be needed to connect E_{eff} with

the intrinsic anisotropic properties of the material (i.e., single ply) tested. We will revisit this issue a little later in this paper.

The green data in Figure 9C shows several important characteristics which can be used to understand the behavior of the composite. The first is an initial linear segment corresponding to the elastic behavior of the ply being indented. The slope of this segment gives the indentation modulus. The solid gray line indicates this slope in the figure. The correct analysis gives a higher modulus value of 16.77 GPa compared with the value of 13.82 GPa calculated with the lower elastic region. At higher stresses, the stress-strain behavior deviates from the linear indicating the onset of plastic deformation. Here we use a 0.2% offset line (grey dashed line) to calculate a yield point (magenta dot) of 0.42 GPa. Due to the elastic recovery of the matrix, images of the surface after indentation did not show evidence of damage to the surface except for a few small matrix cracks such as the one shown in Figure 10A. Therefore, indentation tests to higher load levels were performed in order to explore the kinds of damage induced by the indentation tests. Visible residual impressions were observed. Figure 10B shows SEM images of the surface after indentations using the same tip size but reaching a higher maximum load. Images of the region indented to a high load show expensive evidence of matrix debonding and matrix

cracking. Such deformation mechanisms have also been demonstrated in sharp indentation

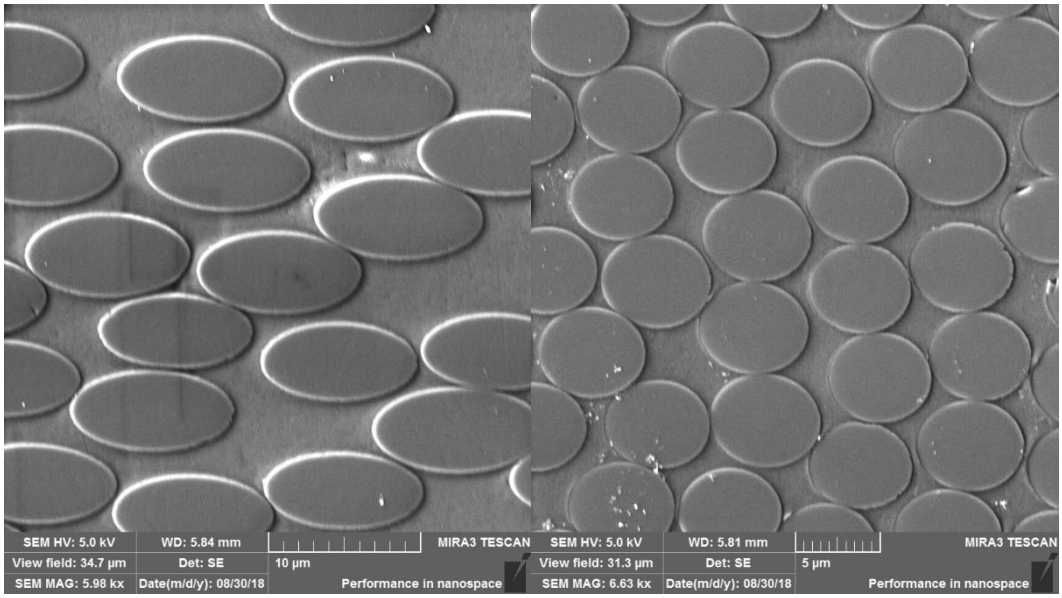

Figure 10: SEM images showing damage to the material surface after indentation. A) shows an indentation location after test conditions showing matrix cracking. B) shows additional damage to the surface caused by a high-load indentation test. Here extensive debonding can be seen around the fibers. Damage to the matrix can also be seen.

tests [68].

The refined and extended spherical indentation stress-strain protocols described in the previous section were employed on plies with fibers at 0 degrees, 30 degrees, 60 degrees, and 90 degrees to the indentation direction. As mentioned earlier, all indentations were performed near the centerline of the plies to avoid any interactions between plies of different orientations. Multiple tests (see Table 1) were run on each ply. The resulting indentation stress-strain curves are presented in Figure 11.

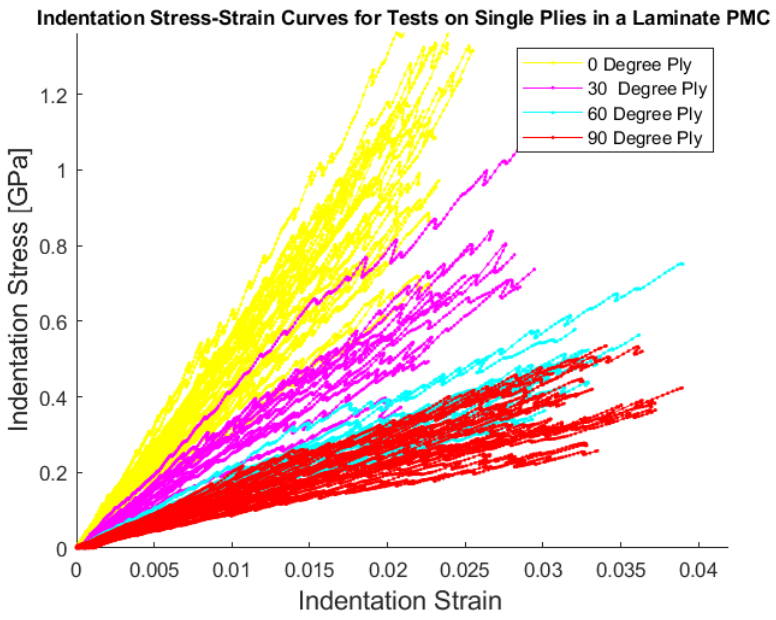

Figure 11: Indentation Stress-Strain curves for indentations in various plies.

The measured indentation stress-strain curves show a clear increase in the values of the indentation modulus (i.e., the slope of the indentation stress-strain curve in the initial elastic regime) with the decreasing declination angle (i.e., the angle between the indentation direction and the fiber orientation in the ply). This is expected because the elastic stiffness of the ply decreases sharply with the declination angle as demonstrated previously in the literature.

A large variance is noted in Figure 11 in the multiple measurements performed in the same ply. We believe that this variance reflects the variance in the mechanical properties in each ply at the length scale of the deformation zone in our indentation measurements. For the measurements reported in this study, this length scale is about 60 μm (corresponding to the diameter of the contact region at indentation yield). In order to

validate the above hypothesis, we have carefully studied the variance in the measured fiber area fractions from randomly extracted images of size 70 μm X 70 μm from serial-sectioned optical images of the plies in our samples. The distribution of the measured fiber area fractions exhibited a mean of 61.8% and a standard deviation of 8.8%. From these observations, it can be seen that the large variance seen in the measurements in Figure 11 could indeed be attributed to the large variance present in the material microstructure in the samples at the length scale of the deformation zone in the indentation tests. We will further validate this hypothesis with FE simulations later.

At higher stress levels, the indentation stress-strain responses deviate from the linear response indicating the onset of permanent (inelastic) deformation. High-resolution images of the unloaded sample (after experiencing permanent deformation) shown in Figure 10A indicate the onset of matrix cracking and fiber debonding in the samples. Similar observations of damage initiation have also been reported in studies that used sharp indenters on the PMC samples [23]. In general, the extent of damage was found to increase with the amount of permanent deformation imposed on the sample (caused by higher indentation loads) as seen in Figure 10B. Here the center of the image roughly corresponds to the center of the indentation zone. It is interesting to note that the majority of the damage, particularly the fiber debonding occurs toward the edges of the image instead of at the center of the indentation. This shift from the center is due to the nature of the stresses found in the indentation zone. A discussion of the nature of the plastic zone during indentation can be found in [31].

A large number of spherical indentations were performed on the multiple plies within the same samples present in the samples prepared for this study. The means and standard deviations for the indentation moduli and indentation yield strengths (using a 0.2% indentation plastic strain offset) estimated from the indentation stress-strain curves are summarized in Table 1. It is clearly seen that both these values decrease sharply with the declination angle. Note that some of the tests with the zero degree declination angle (fiber direction parallel to the indentation direction) did not exhibit plastic deformation. Therefore, the indentation yield values presented in Table 1 were obtained only from the tests from which an indentation yield point could be extracted reliably.

Table 1: Measured values of modulus and yield for indentation tests in various angle plies.

Plies	Number of Tests	Average Modulus	Modulus Standard Deviation	Average Yield	Yield Standard Deviation
0 Degree	**29**	**43.236**	**8.7268**	**1.1645**	**0.2267**
30 Degree	**14**	**29.93**	**3.9962**	**0.70073**	**0.22676**
60 Degree	**18**	**16.573**	**1.6792**	**0.40552**	**0.18026**
90 Degree	**28**	**12.397**	**2.9926**	**0.29473**	**0.08393**

Surprisingly, the values of the measured indentation moduli reported in Table 1 are significantly lower than the previously reported values of the compression moduli for the same plies. As already mentioned, the compression moduli for the plies have been reported to be 137 GPa and 8.69 GPa in directions parallel and perpendicular to the fibers. In order to understand this difference between standard uniaxial tests (e.g., tension, compression) and indentation tests, it is necessary to conduct finite element simulations of the spherical

indentation tests. Indeed, FE simulations have been used extensively in prior literature [78-81] to help interpret the measurements conducted in the spherical indentation tests.

FE simulations have been used extensively in prior literature [48-51] to help interpret the measurements conducted in the spherical indentation tests. In the FE models used in this work, the sample material is treated as a homogeneous material exhibiting transversely isotropic elastic response. The transverse isotropy is prescribed using a material reference and five elastic stiffness denoted as $\{C_{11}, C_{12}, C_{33}, C_{13}, C_{44}\}$ based on calculations from the epoxy and fiber properties using Eqs. 8-12.

$$E_3 = E_{f3}V_f + E_mV_m \tag{8}$$

$$E_1 = E_2 = \frac{E_m}{1 - \sqrt{V_f}(1 - {E_m}/{E_{f2}})} \tag{9}$$

$$G_{23} = G_{13} = \frac{G_m}{1 - \sqrt{V_f}(1 - {G_m}/{G_{f23}})} \tag{10}$$

$$G_{12} = \frac{G_m}{1 - \sqrt{V_f}(1 - {G_m}/{G_{f12}})} \tag{11}$$

$$v_{23} = v_{f23}V_f + v_mV_m \tag{12}$$

As noted earlier, the fiber volume fractions in the deformation zones in our indentation experiments are likely to have varied between 50% and 70%. Using these volume fractions in the models suggested by Chamis [52], we estimated the lower bound for the effective

ply stiffness to be ($C_{11}, C_{12}, C_{13}, C_{33}, C_{44} = 11.3, 5.4, 5.4, 143.1, 3.7\ GPa$), while the upper bound values were estimated to be ($C_{11}, C_{12}, C_{13}, C_{33}, C_{44} = 18.1, 10.2, 8.7, 199.6, 5.7\ GPa$).

The FE mesh for the present work has been adopted from prior work [49] by Andrew Castillo. The FE model assumed a frictionless contact between a rigid spherical indenter and the anisotropic elastic sample (specified using the five elastic stiffness parameters described above). Simulations were performed for 0, 30, 60, and 90 degrees of declination angles (using suitably oriented material reference frames).

All of the FE simulations performed in this study produced linear indentation stress-strain curves when analyzed using Hertz's theory, once again confirming that a linear relationship continues to exist between P and $h_e^{3/2}$ (see Eq. (1)) even for the highly anisotropic case of PMC laminates. As mentioned earlier, this is a significant result and justifies the use of Hertz's theory in the extraction of indentation stress-strain curves even when the sample exhibits very high levels of elastic anisotropy. Of course, one still needs to establish a meaningful interpretation of the extracted value of the indentation modulus for anisotropic materials. In this work, we get around this challenge by using the exact same protocols for the extraction of the indentation stress-strain curves from FE simulations as we did in the indentation experiments. This allows us to directly compare

the measured and FE predicted indentation moduli for the different ply orientations studied in this work.

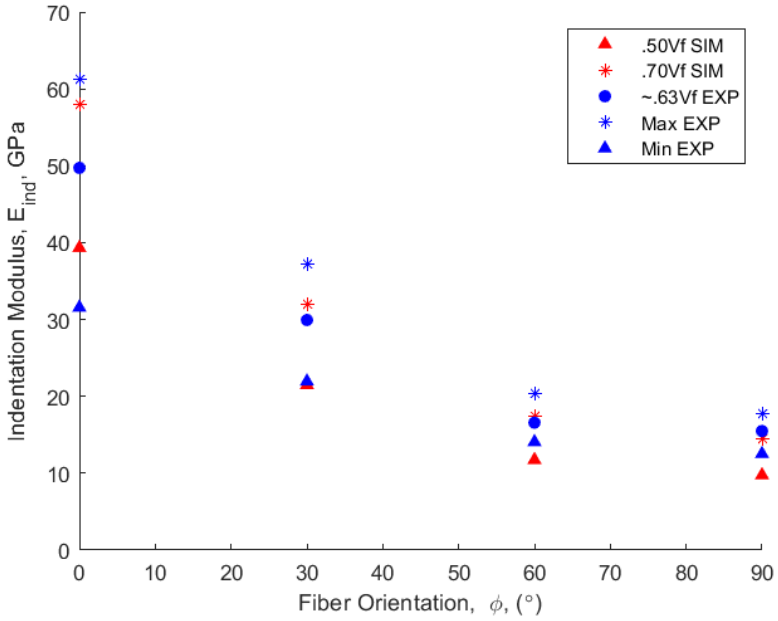

Figure 12: Comparison of experimental results of modulus with the results of simulations of the indentations.

The FE predicted indentation moduli are compared with the corresponding experimentally measured indentation moduli in Fig. 9. The simulated indentation moduli corresponding to a lower fiber volume fraction (50%) are consistently lower than the higher fiber volume fraction (70%), providing estimated bounds for the experimentally measured indentation modulus. Both experimental and simulated indentation moduli follow a trend of decreasing indentation modulus with increasing declination angle. Furthermore, the experimentally measured mean indentation modulus (see Table 1) consistently falls within the bounds provided by the finite element simulations with the exception of the highest declination angle. This result implies that some of the testing was performed in areas with volume

fractions somewhat higher than the simulated 70%. An interesting note is a difference between the simulated indentation moduli of the selected fiber volume fractions tends to increase at lower declination angles. This observation suggests that, for the set of constituent fiber and matrix elastic parameters used to estimate the effective ply properties, the resulting indentation modulus has a relatively higher sensitivity to variations in fiber volume fraction at lower declination angles. This observation is consistent with the experimentally reported values, as the range of experimentally measured indentation moduli consistently increases at lower declination angles (local fiber volume fraction at indentation sites vary for a single declination angle). The deviation from the simulated indentation modulus at highest declination angle, as well as the differing ranges of reported indentation moduli values at lower declination angles, suggests fine-tuning of the effective elastic constants may be appropriate to arrive at more concise bounds for effective ply properties. Such an effort should rigorously consider the apparent uncertainty of the experimentally measured indentation moduli at the different declination angles and will be pursued in future work.

4.4 Conclusion

This paper has demonstrated the applicability of the updated stress-strain protocols to the study of Carbon Fiber/Epoxy laminate composites at the single ply lengthscale. It has been demonstrated that variance in the local properties exists between the lamina at different angles as well as within a single lamina. Within a single ply, this variance is shown to be a result of local variation in the volume fraction of the fibers. The amount of variation between tests in a single ply is consistent with the results from finite element simulations

of the indentation. Since the simulations were based on the angle of the fibers with the direction of indentation and the volume fraction of the fibers, it can be concluded that these two factors play a large role in the variation in properties on the local scale. This consistency is also evidence to verify that the protocols are capable of accurately capturing the local properties of the material. Equally as important it has been shown that the nanoindentation tests can be used to initiate damage in PMCs and that damage can be quantified as the local indentation yield point of the material. This paper has demonstrated that indentation tests induce both fiber debonding and matrix cracking. Future work could focus on using these tests to extract post-yield behavior to inform damage models of composites.

CHAPTER 5. INDENTATIONS ON NANO-COMPOSITES

5.1 Introduction

Nano-composites have the capability of drastically increasing the properties of the composite compared to the neat polymer without significantly changing the weight or processing pathways. In particular, carbon nanotubes (CNTs) show great promise due to their high aspect ratio and mechanical strength as well as unique electrical and thermal properties. Barriers to implementation of such materials in advanced applications are due to changes in the materials during processing (such as waviness) and agglomeration of the tubes within the composite. In order to understand how these materials change during processing and to optimize processing conditions, it is important to know the properties on the local scale. Preferably methods for testing such local properties would need to be able to be done on the material in the shape it will be used in as processing into different shapes can cause variations in the properties. Such a test method would also need to be high-throughput so that many locations could be tested giving a statistical representation of the material and highlighting areas of the variance in the properties. Therefore, indentation testing presents itself as an optimal solution for measuring these local properties.

It is critical that a thorough understanding of the composite properties be established to improve and expand composite models for arbitrary shapes and loading conditions. This paper will explore the use of instrumented spherical indentation stress-strain protocols to study the mechanical properties of polypropylene and carbon nanotube composites. The differences within and between samples with different loadings of CNT will be examined.

Then the results will be compared with the results of tensile testing on samples with the same processing history. This paper will demonstrate the applicability of the recent indentation protocols for determining the variance in the mechanical properties in the selected polymer composite materials. Use of these protocols on a variety of composite materials will allow for greater predictive power in models refined by these results.

5.2 Materials and Samples

As previously reported in Bhuiyan et al. [83] the polymer used to create the samples is a PP powder (Pro-fax 6301, melt flow index 12g/10 min), purchased from Basell. The multi-walled carbon nanotubes were purchased from Cheap Tubes, VT, USA and were used as reinforcement. As per the supplier, the specifications of the nanotubes are as follows: outer diameter 20-30 nm, inner diameter 5-10 nm, length 10-30 um, purity >95 weight % and ash <1.5 weight %. The composites were fabricated by extrusion and injection molded to form dogbone shapes. A DSM Micro 15 cc Compounder and 10 cc injection molding machine were used for melt mixing and injection molding respectively. The materials were compounded at T_{barrel} = 180 ºC for 3 mins with a screw speed of 245 rpm. The material was injected into the mold at T_{mold} = 80 ºC with an injection pressure of approximately 758 kPa. Samples were created with 0 wt.%, 1 wt.% and 5 wt.% loading of CNTs. These

loadings correspond to 0 vol%, 0.48 vol% and 2.46 vol% respectively. Figure 1 shows a reak surface SEM image of the composite material.

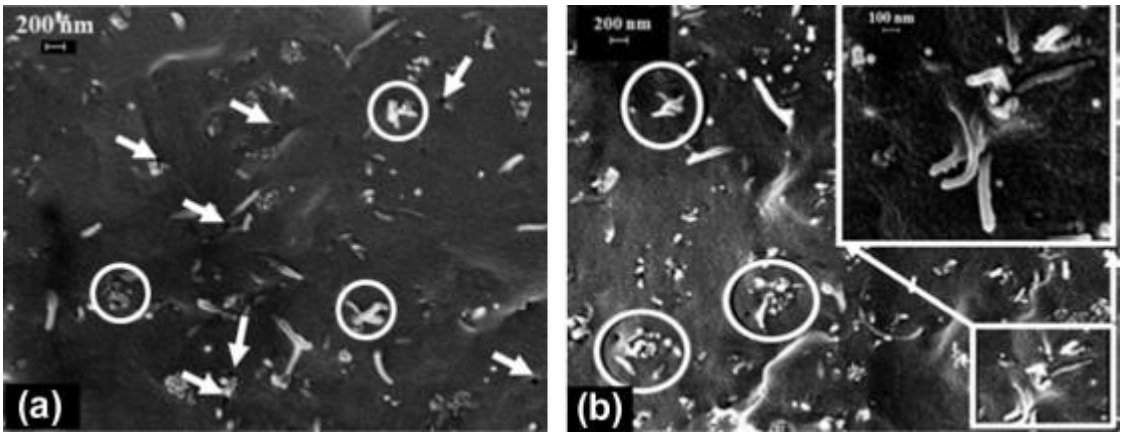

Figure 14: Fracture surface imaged in the SEM clusters of CNTs are shown with the circles and boxes show waviness of the CNTs. Originally published in Bhuiyan et. al.[79] Used with permission.

From these images, it can be seen that CNTs are inhomogeneously dispersed. Therefore, we would expect the local properties to also have a high degree of variation. The ability to characterize this variance is one of the strengths of using the nanoindentation tests.

From the dogbone samples, a sample was taken from the gauge section. This sample was then mounted in an epoxy mount for polishing and indentation. Care was taken to orient the sample such that indentations could be performed in the direction of the flow of the material into the mold. Figure 12 shows the direction of the indentation relative to the

sample. This orientation allows for the most direct comparison with a tensile test to account for any directional effects caused by the alignment of the nanotubes in the sample.

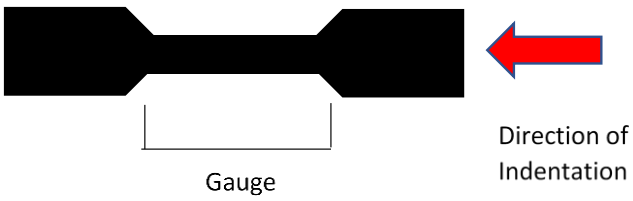

Figure 15: Schematic depicting the dog bone sample from which samples for indentation were cut. The arrow indicates the direction from which the indentations were performed.

5.3 Surface Preparation

Samples were cut from the gauge section and mounted in epoxy. Then, samples were prepared according to the preparation method described in Abba[84] with slight variations in time for each step based on the needs of the sample. Optical images of the polished surface were taken between each step to discern if the time employed on that step was sufficient to get rid of the polishing scratches from the previous step. If not, polishing on that step proceeded in one-minute increments. In addition, as a final step for each sample, ion milling was used to finish the surface. A Hitachi IM4000 Plus Ion Milling System was used. The milling was performed with a tilt of 80º with no eccentricity. The operation mode was F2, which rotates the sample at 25 rotations/min with a swing angle of 360º. The mill was performed with an acceleration voltage of 3kV and a discharge voltage of 1.5 kV for up to 30 minutes in 5-minute increments. After this step, samples were deemed suitable for use in indentation tests based on optical images of the sample.

5.4 Steps of Applying the protocols to Nanocomposites

As discussed in chapter 3, it is important to make sure that the analysis of the indentation data is accomplished carefully so as to obtain the correct material response. There are several factors to consider. The first is the viscoelasticity of the material. This can be approached by running the tests at a high rate such that the instantaneous response of the material is probed. This work uses a strain rate of 0.5 s^{-1} as measured by the software native to the indenter. This strain rate is approximate as the machine uses estimates for the contact area. This rate was chosen as higher rates gave the same response.

The aspect of the analysis that is important to be careful to choose correctly is the choice of the elastic segment. As indicated previously, this choice of the segment is highly important as it will influence the stress and strain calculations significantly. For these samples, the correct choice of the elastic segment can vary from test to test. The first reason is that the nanoindenter can register false contact. The nanoindenter determines contact with the surface based on a change in the stiffness signal. However, due to the low mechanical stiffness of the material, these settings must be set to a lower value so that the contact is not missed. However, this sometimes results in the false identification of the contact point. This can be seen in the low load region of the curve. In many samples, a very low load is shown to persist for a significant amount of displacement. Once the indenter is truly in contact the load begins to increase as normal. The initial elastic segment must be chosen after this initial portion. The second reason that the choice of the elastic region is challenging is the variation within the material. As with the carbon fiber example, the size of the contact rapidly changes in the initial portion of the test. As the material is

not homogeneous, the contents of the initial volume will be variable. At some point, the contact will be large enough to be considered representative of the local area. Figure 3 shows a plot corresponding to the various steps in the analysis of the load-displacement data to produce the stress-strain curves. Part C, the zero-point fit plot, is the first indication that a chosen segment is indeed elastic. This plot is based on the Hertz equation relating the load-displacement and stiffness response of the material. An elastic segment will be linear on this plot. This plot shows three distinct regions: an initial curved region, a linear region indicated in green and then a final region where the behavior is more erratic. The second region is where the elastic segment can be found. Once an elastic segment has been chosen, it is important to check that the modulus fit is also linear. Based on these observations, an appropriate analysis can be chosen.

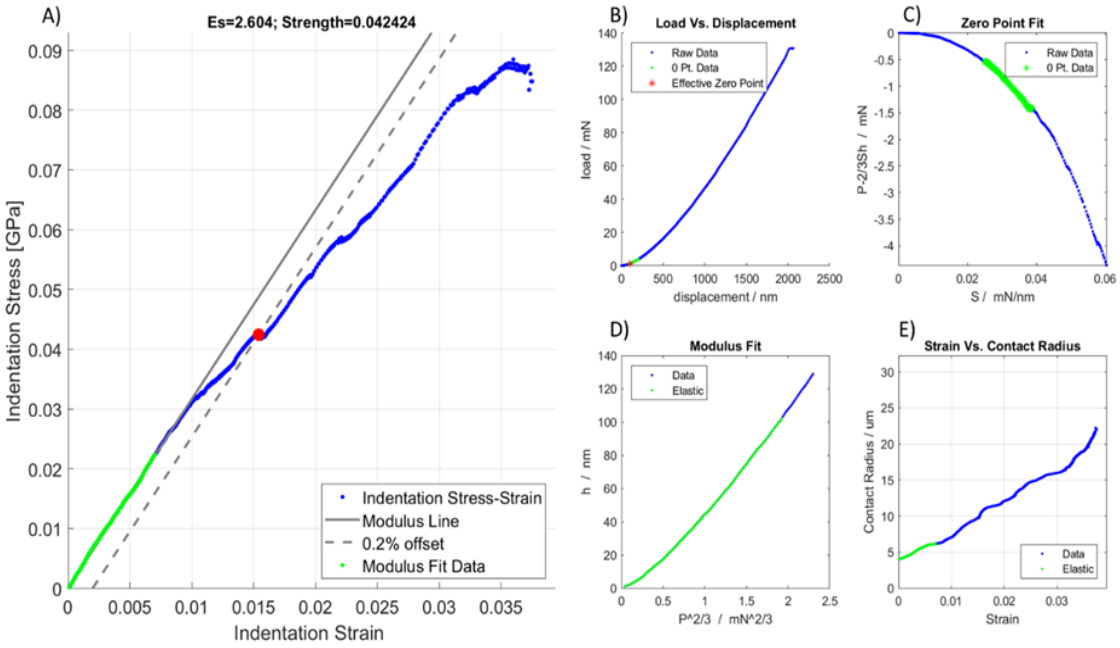

Figure 16: Steps for the stress-strain analysis of indentation data. A) shows the final stress-strain results. The green points in all the graphs indicate the initial elastic segment chosen for analysis. The red dot indicates the yield point as determined by the 0.2% offset (grey dotted line) B) shows the raw load-displacement data. C) shows the plot used to determine the effective zero-point. D) shows the plot used to calculate the modulus. E) shows the calculated contact radius which is used to determine the stress and strain. For more information on these steps please see chapter 3.

5.5 Results

5.5.1 Raman

As the CNTs could not be reliably imaged on the polished surface, Raman spectroscopy was used to characterize the variance in the carbon nanotubes. Spectra were gathered from various locations on the surface of the 0, 1wt%, and 5wt% samples. Spectroscopy was

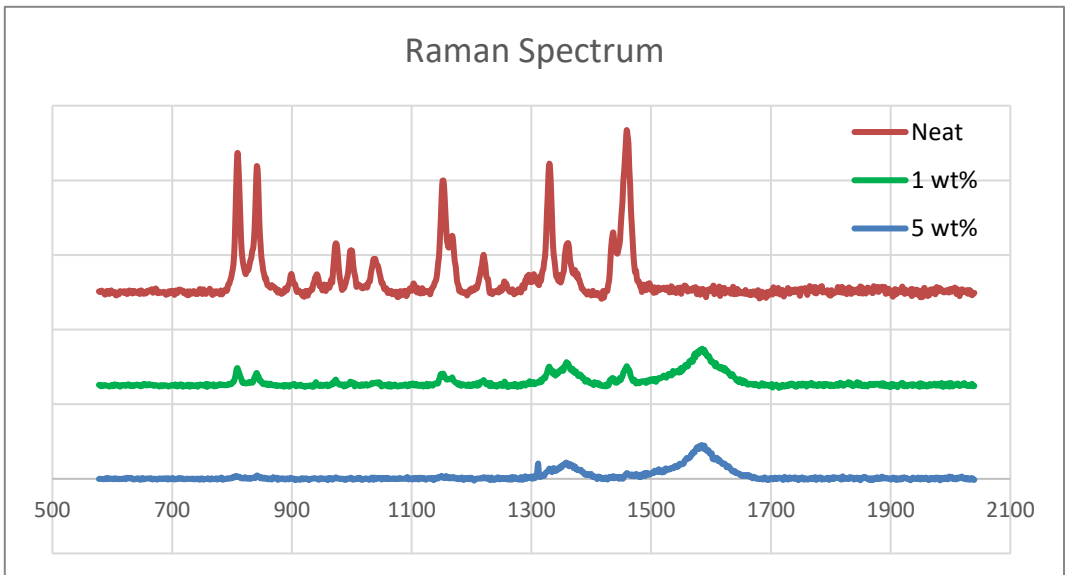

Figure 17: Individual Raman results for the 0, 1 and 5 wt% samples. Note the peaks indicating the presence of polypropylene at 808 and 840 cm^{-1}. The peak which most strongly indicates the presence of carbon nanotubes can be found at 1593 cm^{-1}.

performed with a Renishaw Qontor Dispersive Raman Spectrometer equipped with a 488nm and a 785 nm laser. The 488 nm laser was chosen for this testing as it gave a better signal to noise ratio particularly for the polypropylene peaks in the 5% samples where they are more difficult to distinguish. The test was run using a 20X objective with 0.5% laser power and an exposure time of thirty seconds. These settings were chosen as they gave the shortest measurement time while preventing damage to the surface. In particular, using a higher laser power caused significant damage to the surface. Figure 17 shows a result from each of these samples plotted together. Intensities were shifted so that the details of each spectrum could be seen. While many of the peaks overlap, The CNT peak at 1593

cm^{-1} and the PP peaks at 808 cm^{-1} are independent of the influence of the other material respectively. Therefore, these peaks can be used to look at the variation in the amount of each respective material from different locations. Raman spectra were taken from random locations on the surface of the sample to show the variance in composition. For the 5% sample, the intensity of the CNT peak ranged from 378.7 to 787.9 counts with an average of 681.3 and a standard deviation of 137.4. The PP peak ranged from 10.0 to 55.5 counts with an average value at 47.0 and a standard deviation of 22.0. The 1% sample showed smaller variation in the CNT peak ranging in intensity from 587.1 to 716.7 counts with an average of 637 and a standard deviation of 36.9. However, the PP intensities showed greater variation ranging from 203.8 to 425.5 counts with an average of 302.7 and a standard deviation of 93.9. The greater the degree of variation shifts from the CNT peak to the PP peak when going from 5wt% to 1wt% as the CNT peak significantly overpowers the PP peak in the 5wt% sample. The presence of variance in peak intensities at different locations indicates the presence of a large amount of inhomogeneity within the sample which will also be reflected in the local properties.

5.5.2 Indentation Tests

Samples with loadings of 0, 1 and 5 weight percent carbon nanotubes were indented with a 500 μm spherical indenter. Each of these tests was analyzed according to the protocols elaborated on earlier. Figure 18 is a graph the results of 15 different tests on the 5 wt%

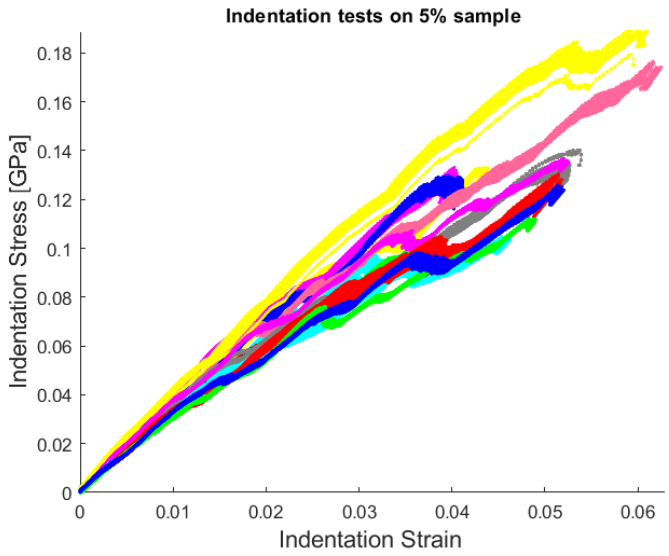

Figure 18: Indentation tests on 5 weight percent sample.

sample. One important attribute of this data is the amount of variation between the different tests. This variation is due to the differences in the percentage of the CNTs within the contact region. The size of the contact region ranges from a 5 μm radius to 25 μm radius

Table 2: Indentation Modulus and Yield values for tests on PP/CNT samples.

500 um tests	Average Modulus (GPa)	Modulus Standard Deviation	Average Yield (MPa)	Yield Standard Deviation
Neat PP	2.5499	0.25237	44.168	6.88
1 wt% PP/CNT	2.7417	0.24557	61.354	17.321
5 wt% PP/CNT	3.0537	0.26956	54.526	12.514

area during the course of the test. A similar level of variation is evident in the other samples. Such variation is indicative of heterogeneity at the scale of the 500 μm test.

Such heterogeneity is evident in both the variation in intensities in the Raman results and in the SEM image in Figure 14. Although the size of the clusters is smaller than the indentation zone size, the spacing between them is on the same order as this size. As a result, the indentation tests could be performed on areas containing CNT aggregates with high volume fractions of CNTs or on areas with mostly polymer. This variation in local structure leads to a variation in local properties as well.

Table 2 shows the average results of the modulus and yield calculations from the stress-strain curves. It should be noted that while the modulus is naturally increasing with the

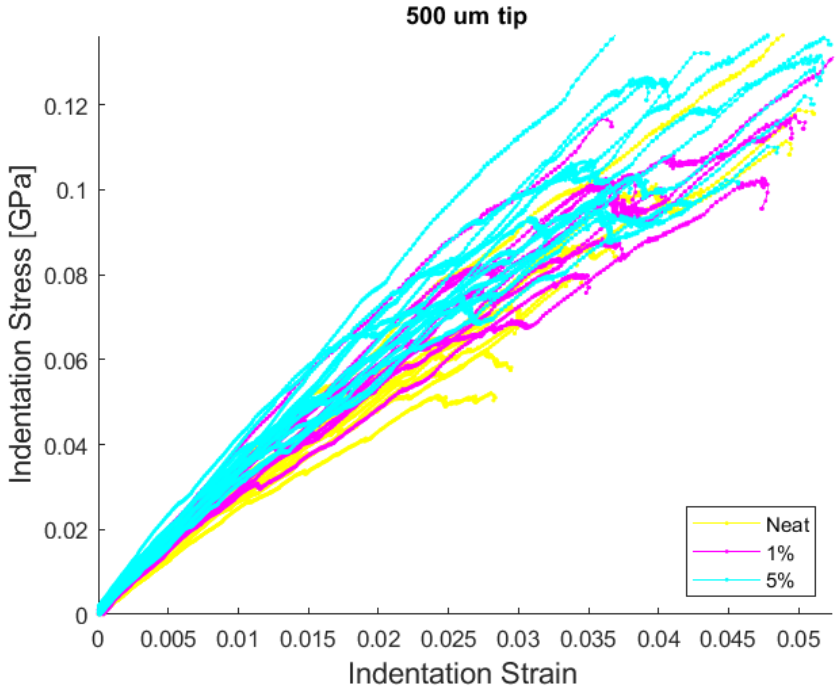

Figure 19: Indentation test results on neat 1wt% and 5wt% PP/CNT samples. Indentations were taken from a variety of locations across each sample.

increasing weight percent of the CNTs, this increase is on the range of the variance in the modulus from the various tests. This is due to the fact that many of the tests may be falling on areas that range in volume fraction of the CNTs from all polymer areas to the high concentration of CNTs in the CNT. Figure 19 shows the indentation stress-strain plots for better visualization of this variance and its overlap.

The variance in the properties of the material is due to the heterogeneity of the material. Within the contact region, the amount of CNT varies significantly. Such variance needs to be understood in order to improve the manufacturing efforts. Use of indentation tests to characterize the variance in the properties can lead to better manufacturing processes.

5.6 Conclusion

This work has shown the application of analysis protocols for extraction of stress-strain curves from an indentation test for polypropylene carbon nanotube composites. It has been demonstrated that the variation in mechanical properties due to the inhomogeneity of the composites can be captured. This variation has been shown to be on the same order as the differences in mechanical properties due to differences in loadings of carbon nanotubes.

CHAPTER 6. CONCLUSIONS AND FUTURE WORK

6.1 Conclusions

This work has shown the viability of these indentation protocols to determine the local modulus and yield point for polymer matrix composites. Two different material systems have been tested and analyzed to determine the viability of these protocols. The first was a multi-laminate composite where the properties within individual lamina were calculated. The second was carbon nanotube nanocomposite. In this process, some important points were determined which are critical for the analysis of composite materials.

1. The careful preparation of the sample surfaces is critical to the accurate examination of the composite properties. Due to the differing nature of the components of the composite care must be taken when preparing the surface for indentation. Some methods for preparation differentially eroded the different components leading to a height difference which led to the incorrect identification of the effective zero-point. With careful preparation, this discrepancy was lowered to a reasonable level such that the effective zero-point could be determined.
2. The second important point that was gleaned from the development of these protocols is the importance of correctly determining the elastic region for calculation of the effective zero-point. This region must be when the indenter is fully in contact with both components of the composite. This requirement means that the slight height difference that remains after careful sample preparation must be taken into account when choosing the elastic region. Another important

consideration when choosing the elastic region is determining that the indenter is in contact with enough of both components that the for the response of the material to be considered representative of the composite region and not an individual component.

3. The final point that was important to this work was that these protocols can be used to characterize the variation in properties at the local scale. This point can be seen in the differing amounts of variation that can be seen when using different indenter sizes. The increased variation at lower length scales was due to clusters of components which were homogenized at the higher length scales. Careful choice of the indenter size can lead to an understanding of the variance in properties at various length scales.

6.2 Future Work

This work has shown the viability of these protocols for polymer composites at intermediate lengthscales but there is much work to still be accomplished. These protocols need to be applied to other composite structures to prove their viability on a variety of PMCs. Such alternate materials could be weave structures or short fiber composites. Both of these have distinct lengthscales and modeling of these structures would benefit from the application of these protocols.

In addition, these protocols can be used to provide data for the building of structure-property linkages and the building and validation of various models. Work needs to be done on communication with modeling experts as to what data is most important to be

extracted from the data provided by these protocols. Some preliminary work has been done in the creation of structure-property linkages in composite materials and can be reviewed in Appendix A. Improving this work by using the data determined by the protocols which were the focus of this thesis to create the structure-property linkage is an important step forward for this work.

APPENDIX A. ROBUST PROPERTY STRUCTURE LINKAGE FOR POLYMER COMPOSITES

A.1 Background

Fiber-reinforced composites have become increasingly important structural materials, particularly in the automotive and aerospace industries. The property enhancement afforded by the use of a fibrous reinforcement allows for lightweight high-performance parts. The effective mechanical and functional properties of composites are generally modeled using highly sophisticated homogenization theories[86] However, most practical approaches found in literature employ simpler idealized models that are heavily customized for specific classes of composites. For example, Hallal et al.[87] published a review of the different types of models used to estimate the properties of the woven structures. Each model works well for the composite class (usually defined based on reinforcement structure) for which it was designed. Such models perform poorly when applied to other structures. As other examples, composite models have been proposed for short fiber reinforcement[88, 89], long fiber reinforcement[90, 91], and continuous fiber reinforcement.[92] For example, one commonly used model for short fiber reinforcement, the Halpin Tsai model falls short in long fiber reinforced materials and in high volume fraction of fiber samples. Although there are many models that fit these idealized structures under certain conditions, in practice, real fiber composite structures fall between idealized structures, making it often unclear as to which models should be applied in a particular application. For example, it has been shown that long fibers can break up during injection

molding[93]. This break-up of the fibers results in a structure that contains fibers lengths that span the spectrum from the small fiber range (0.2-0.4mm) to the long fiber range (10-13mm). Therefore, a single idealized model would not be capable of modeling the entirety of the structure.

A model that is capable of predicting effective properties for a broad range of reinforcement morphologies in composite materials currently does not yet exist. Such a unified model would need to rely on a comprehensive set of metrics for the composite microstructure that is relevant to all classes of reinforcement morphologies of interest. Recently, an open science infrastructure for creating objective linkages between statistical representations of the material hierarchical structure and its associated effective properties has been developed[94, 95]. In this paper, this framework is applied to the creation of a microstructure-sensitive linkage for a very broad class of composites including a variety of reinforcement morphologies and spatial arrangements.

A.2 Methods

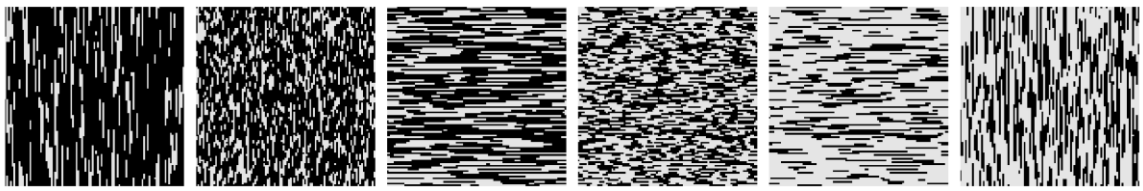

Figure 20: One instance from each of the 2D microstructure classes generated for this study. The volume fraction, orientation, and length of the fibers were varied. The aspect ratio of the fibers starting from the left are 20: 1, 5: 1, 1: 20, 1: 5, 1:15, and 15: 1 while the volume fractions for each of the subclasses were around 20%, 30%, 40%, 50%, 60%, and 70% with a ±10% variation.

A.2.1 Data Generation

A broad range of two-dimensional (2-D) microstructures with a size of 101 x 101 voxels were generated using the open source python library Materials Knowledge Systems in Python (PyMKS).[96] Three specific parameters within the PyMKS microstructure generating functions were varied to create different classes of microstructures: i). fibers of different lengths were created with aspect ratios of 20:1, 15:1 and 5:1; ii). the orientation of the fibers was varied to be either parallel or perpendicular to the loading direction, and represent the extrema of mechanical properties of the composite material with reference to the loading directions, and iii). the volume fractions of the fibers were varied from 10% to 80%. The locations of the fibers and the exact volume fraction are selected using stochastic processes to represent the variance found in real structures. In total, 1200 microstructures were generated consisting of 6 subclasses of 200 microstructures each. An example of each of the 6 subclasses can be found in Figure 6.

The effective stiffness values were computed using the finite element simulation in PyMKS. The simulation uses the periodic boundary conditions to solve the elastostatic equation for displacement described in Eq. 13.

$$\mu u_{i,jj} + (\mu + \lambda) u_{j,ij} = 0 \tag{15}$$

In Eq. 13, u is the displacement vector field, L is the length of the square domain, $\bar{\varepsilon}_{xx}$ is the average or macroscopic applied strain, and μ and λ are defined in terms of the Young's Modulus E and Poisson's ratio ν as shown Eq. 14 and Eq. 15.

$$\lambda = \frac{E\nu}{(1-\nu)(1-2\nu)} \tag{16}$$

$$\mu = \frac{E}{3(1+\nu)} \tag{17}$$

In the simulation, the property values were chosen to simulate a polypropylene and glass fiber composite system. The Young's modulus and Poisson's ratio values were 1.3 GPa and 0.42 respectively for the matrix and 75 GPa and 0.22 respectively for the fibers. These property values were chosen to simulate a polypropylene glass fiber system. The macroscopic imposed strain was set equal to 0.001.

A.2.2 Workflow

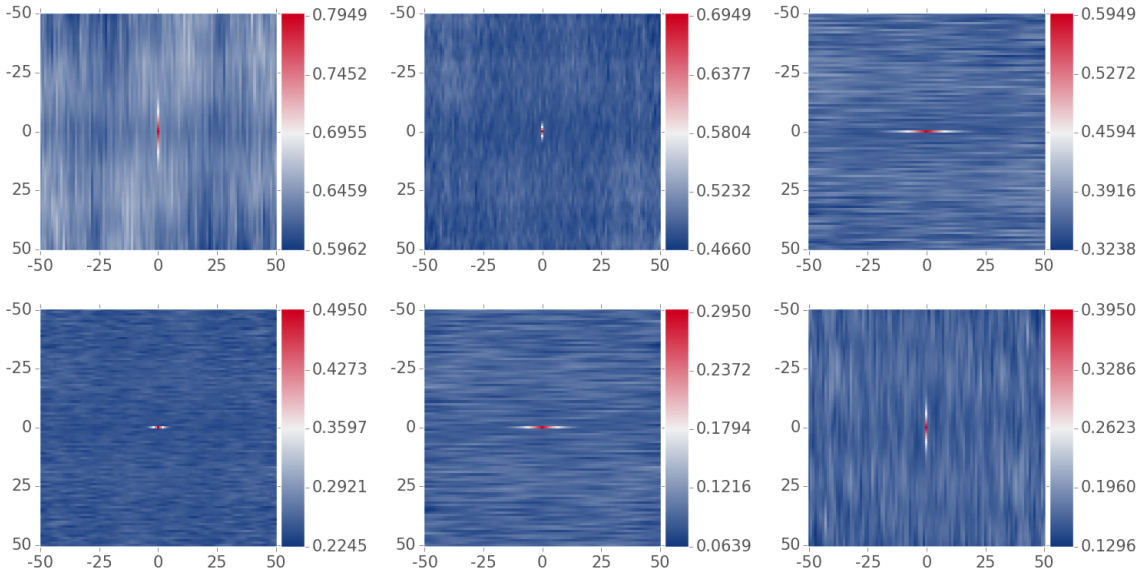

Figure 21: Autocorrelations with fibers for each of the structure shown in Figure 16. The top three autocorrelations correspond to the three structures on the left and the bottom three correspond to the three structures on the right. The tick marks on the x- and y-axes represent the location of the head of a vector with its tail at the origin.

A workflow was established to create a linkage between the fiber composite microstructures and the properties of these fibers. This workflow allows for the replication of this work with other materials systems. The basic steps of this workflow are a quantification of the microstructure with statistics, reduction of the dimensions to the most salient features, and regression and optimization. Each of these steps will be explained in more detail in this description. In this case study, the quantification of the microstructures was done using 2-point statistics[94, 95, 97-99]. 2-point statistics are a set of probability density functions which capture the spatial distributions of local states (in this case phases) within the material structure and embed a large number of conventional measures typically employed by domain experts (including measures such as volume fraction, dominant orientations, average interface area per unit volume).

In addition to capturing the salient features in a microstructure, 2-point statistics provide a natural origin or a point of reference to compare the microstructures. To illustrate this point, autocorrelations of the reinforcement phase (one set of 2-point statistics) for each structure found in Figure 6 are shown in Figure 7. The top autocorrelations correspond to the three microstructures on the left while the bottom autocorrelations correspond to the microstructures on the right.

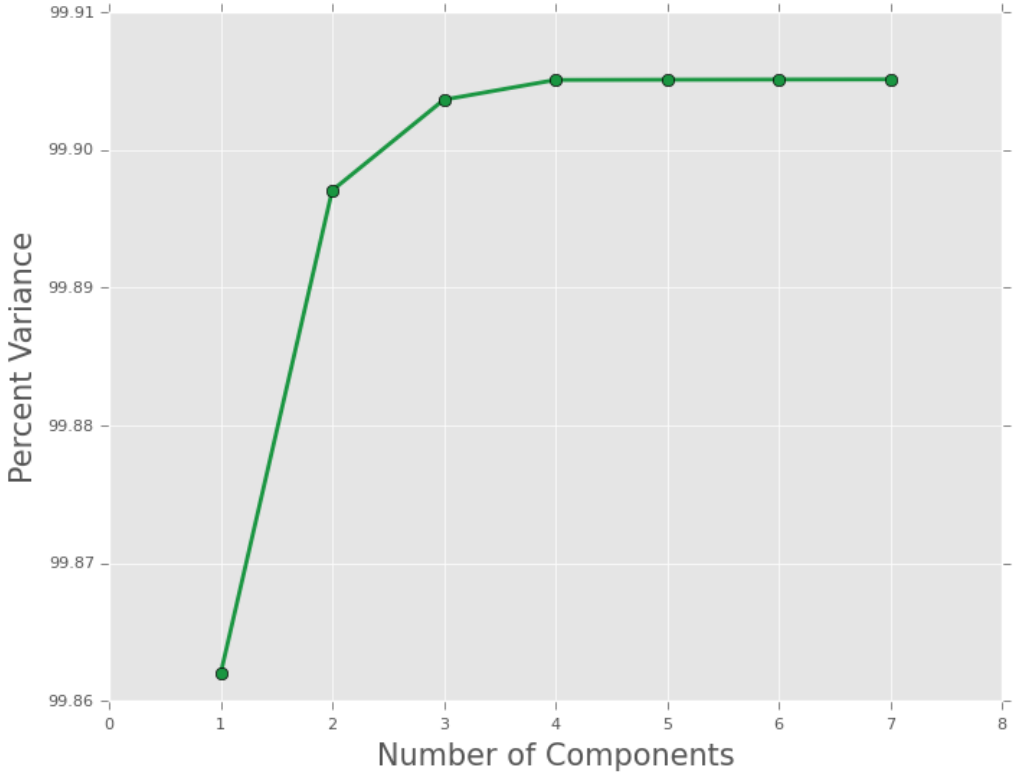

Figure 22: The percent variance as a function of principal components computed using Principal Component Analysis (PCA) on the 2-point statistics for each microstructure.

The computation of 2-point statistics results in an extremely large feature space (with 20402 total features as a result of the number of voxels and sets of 2-point statistics) that is unwieldy to create linkages between microstructures and effective properties. Therefore a method must be used to reduce the dimensions of the space. Principal component analysis (PCA) was used to reduce the feature space to a small number of microstructure descriptors while preserving almost all the variance in the data as shown in Figure 18. This figure shows that the first few principle components contain almost all of the variance and therefore can be used to represent the microstructure statistics. Figure 19 shows the

distribution of the 2 dominant microstructures descriptors (i.e., the first two PC scores), and demonstrates the remarkable efficacy of PCA in capturing the dominant variance in the microstructure ensemble, and in its objective classification. The separate classes discernable in this plot correspond to the different choices made in the creation of the datasets. The example microstructures shown in Figure 1 have also been added to this figure to show that the separate classes shown in the PC space do in fact correspond to the original classes created. The first principal component correlates largely with the volume fraction of the fibers, while the second principal component correlates with the length and orientation of the fibers.

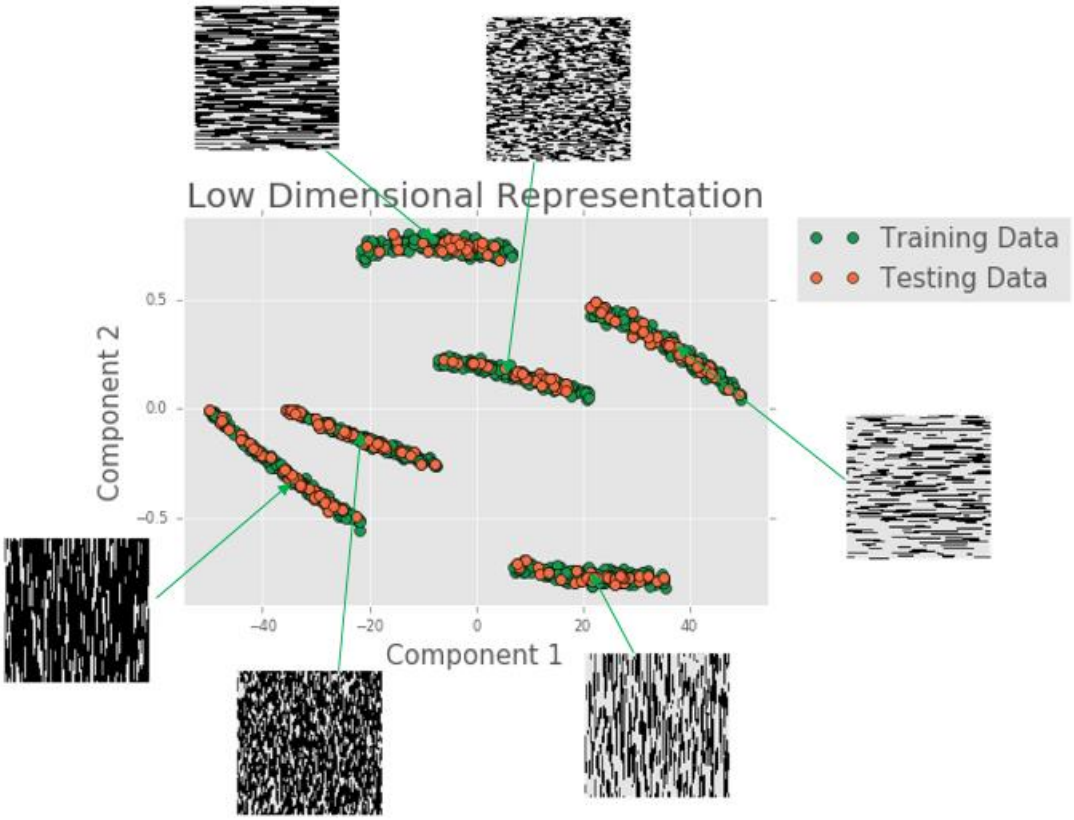

Figure 23: Projection of the microstructure space onto the first two principal components (PC). The first PC correlates with the volume fraction of the fibers while the second PC correlations with the orientation and length and orientation of the fibers.

The set of low dimensional microstructure descriptors found using PCA provides a significantly smaller feature space that can be used in a regression model to create a linkage between the fiber structures and effective properties. Previous studies have shown that polynomial regression using these low dimensional microstructure descriptors can successfully create accurate linkages for varies structures and effective properties[94, 95].

In order to determine the number of microstructure descriptors and the order of the polynomial, the data was split into training and testing datasets. The training dataset was used for parameter selection and calibration of the linkage. The model selection was done by searching the feature space created by varying the degree of the polynomial from 1 to 6 and the number of principal components from 1 to 10. For each possible combination of these parameters, 3-fold cross-validation was used. 3-fold cross validation randomly splits the training dataset into three partitions and calibrates the model with two of the partitions while the remaining partition is used to validate the model accuracy using mean squared error (MSE) as a metric. This process is repeated 3 times leaving out each partition and the average and standard deviation of the MSE values is recorded. 3-fold cross-validation for each parameter combination totaled to 180 calibrations of the model. Figure 20 shows a comparison of the mean and standard deviation of the MSE values. The upper plot shows the log of the mean and standard deviation of the MSE values and the lower plot shows the parameter region that has the most promising results (the range with polynomial degree 2 to 6 and the number of principal components varying from 2 to 5). In the lower plot, the mean values are indicated by the points and the slightly opaque region around the points is the standard deviation. A regression model with a 3^{rd} order polynomial and 4 principal components was found to have the smallest mean MSE with a nominal value of 0.089 and

was used to create the linkage, but there are several value other combinations of parameters that would likely give similar results.

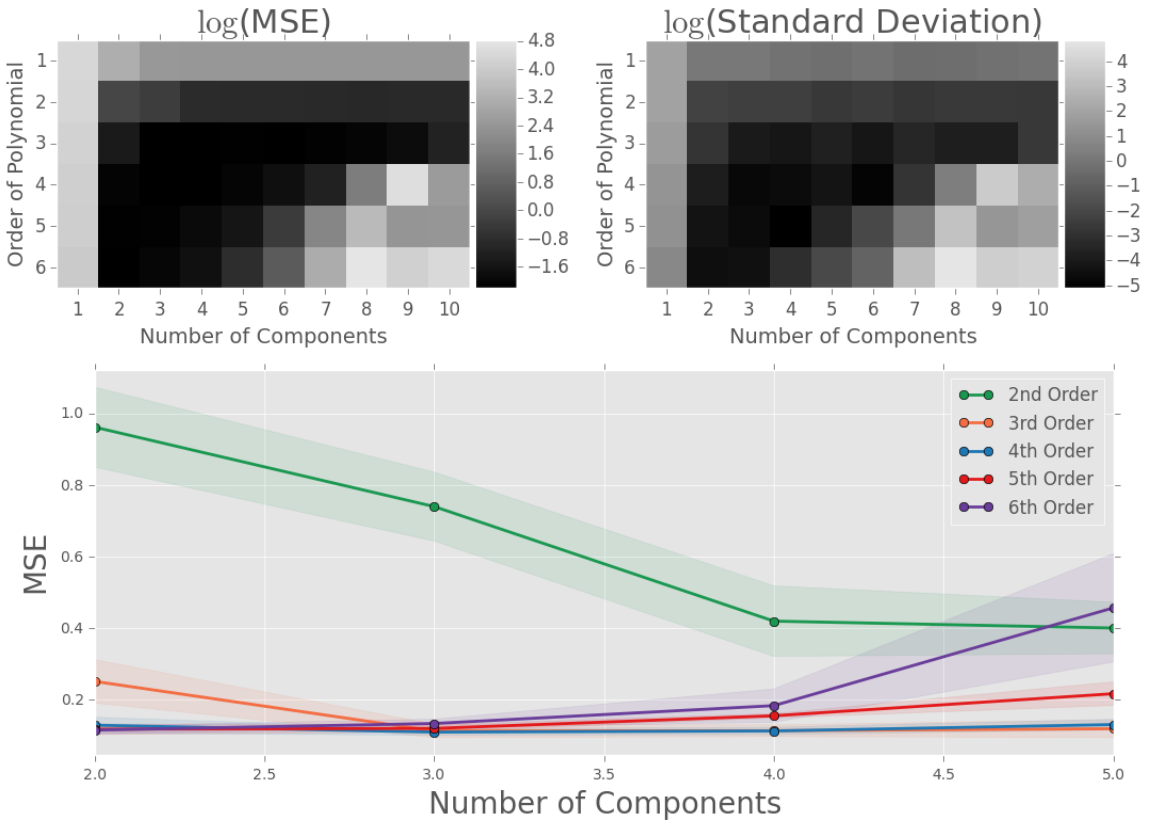

Figure 24: Mean and standard deviation of the MSE values found using 3-fold cross-validation as a function of the number of principal components and the degree of the polynomial regression model. The top plot is the log of the mean and standard deviation of the MSE values. The lower plot shows a subset of the parameter space with the best results with mean of the MSE values indicated with the points and the standard deviation is indicated by the shaded region around each point.

Figure 21 shows a comparison of the effective stiffness value determined by finite element with those predicted by our model for both the testing and training data. The mean percent error for the training and testing data were 1.74% and 1.78% respectively.

Figure 25: Goodness of fit plot of effective stiffness values for both training and testing datasets.

A.3 Results and Discussion

The structure-property linkage created in this study demonstrates that an objective and data-driven framework can be used to predict the elastic properties for a broad variety of composite fiber microstructures as shown in Figure 20. This result compares favorably with the current state of the art found in the literature in several ways. Firstly, this linkage represents a broader range of applicability than the models currently found in the literature.

This linkage is able to identify and reasonably predict the properties of diverse microstructures without labeling of the classes.

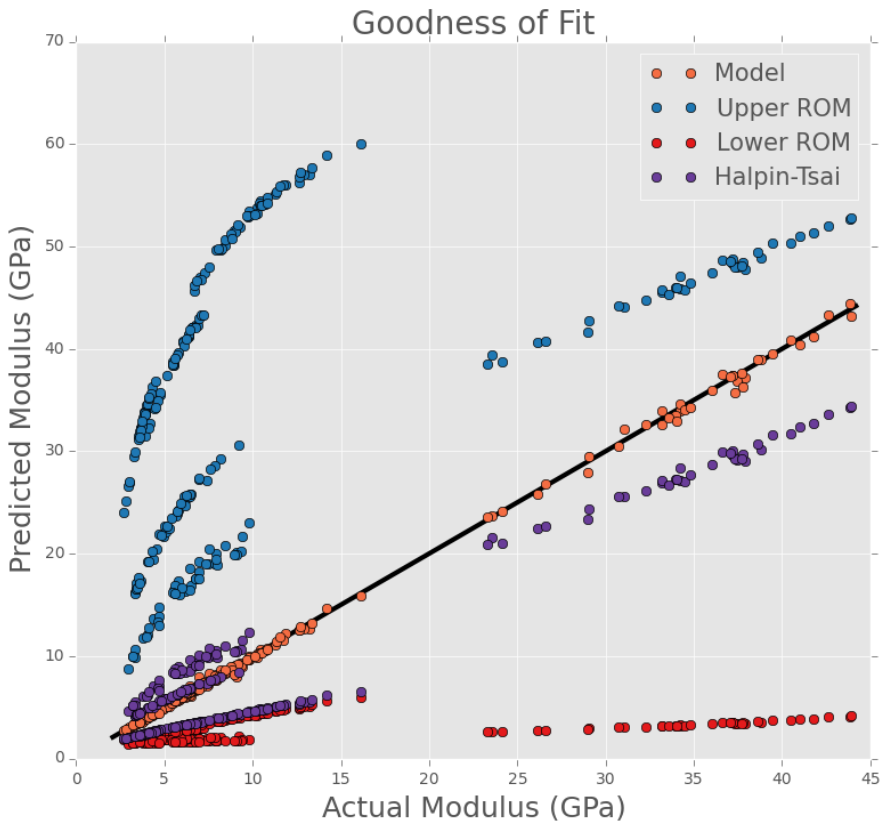

Figure 26: Goodness of fit plot of showing comparison of the new model with standard models for predicting elastic modulus of composite materials. Rule of Mixtures (ROM) and Haplin-Tsai models were applied to the microstructures and the results compared to the FE results.

Secondly, the prediction error compares favorably with the error calculated from existing models. To demonstrate this point, the predicted values from our model along with three models commonly used in practice are shown in Figure 7. Specifically, the upper and lower bound of the Rule of Mixtures (ROM) and the Halpin-Tsai model were used to

predict the modulus of the microstructures. The Halpin-Tsai model estimates the modulus using Eq. 16 and Eq. 17[89].

$$E_L = \frac{1 + \left(\frac{2l}{d}\right)\eta_l V_f}{1 - \eta_l V_f} E_m \tag{18}$$

$$\eta_l = \frac{\frac{E_f}{E_m} - 1}{\frac{E_f}{E_m} + \frac{2l}{d}} \tag{19}$$

In these equations E_L is the longitudinal elastic modulus, l and d are the average fiber length and diameter respectively, V_f is the volume fraction of the fibers, and E_f and E_m are the moduli of the fibers and the matrix respectively. The Halpin-Tsai model was able to reasonably predict the low modulus values, but under-predicted the higher modulus values. This is consistent with comparisons of the Halpin-Tsai model with experiments[8].

Another commonly used model which determines an upper and lower bound on the mechanical properties is the Rule of Mixtures (ROM)[8]. The upper and lower bounds of the ROM are applied using Eq. 18 and Eq. 19 respectively.

$$E_c = E_f V_f + E_m V_m \tag{20}$$

$$E_c = \frac{E_f E_m}{V_m E_f + V_f E_m} \tag{21}$$

In these equations E_c is the composite modulus, and V_m is the matrix volume fraction. All other terms in Eq.18 and Eq.19 are the same as those in Eq. 16 and Eq. 17. Since this is a two phase system, the sum of V_f and V_m must be equal to 1. Figure 22 shows how the predictions of the Rule of Mixtures compare with the Finite Element results. Predictably, Eq. 18 overestimates the modulus and Eq. 19 underestimates the modulus for all the microstructures.

The results shown in Figure 22 clearly demonstrate that the model generated in this work is able to outperform the upper and lower bounds of the ROM and Halpin-Tsai model by accurately predicting the effective stiffness for a broader class of fiber composite microstructures. The model presented in this work clearly advances the modeling of fiber composites compared to the current state of modeling in the literature.

A.4 Conclusion

In this work a linkage which predicts the effective stiffness measures from a wide variety of fiber-based microstructures. This linkage was created from data that was publicly available to be generated. This appendix presented the workflow established for calibrating this linkage and validating it. In addition to comparing favorably with the state of the art in fiber reinforcement modeling, this linkage is easily applicable to a variety of materials systems. Therefore, the methods presented in this paper could be used to generate models for a variety of other reinforcement architectures. Creation of these new models from this workflow would allow an increase in the rate of material deployment by allowing the rapid exploration of large design spaces in material structures. This rapid exploration with allow

for the streamlining of the materials selection process. Ultimately, this process could be instrumental in the acceleration of materials development that has been the focus of initiatives such as ICME and MGI.

APPENDIX B LICENSE

B.1 Rightslink License for the use of Figure 14

ELSEVIER LICENSE
TERMS AND CONDITIONS
Oct 06, 2018
This Agreement between Alicia Rossi ("You") and Elsevier ("Elsevier") consists of your license details and the terms and conditions provided by Elsevier and Copyright Clearance Center.
License Number 4443210035898
License date Oct 06, 2018
Licensed Content Publisher Elsevier
Licensed Content Publication Composite Structures
Licensed Content Title Defining the lower and upper limit of the effective modulus of CNT/polypropylene composites through integration of modeling and experiments
Licensed Content Author Md. A. Bhuiyan,Raghuram V Pucha,Johnny Worthy,Mehdi Karevan,Kyriaki Kalaitzidou
Licensed Content Date Jan 1, 2013
Licensed Content Volume 95
Licensed Content Issue n/a
Licensed Content Pages 8
Start Page 80
End Page 87
Type of Use reuse in a thesis/dissertation
Portion figures/tables/illustrations
Number of figures/tables/illustrations
1
Format electronic
Are you the author of this Elsevier article?
No
Will you be translating? No
Original figure numbers Figure 8
Title of your thesis/dissertation
Mechanical Response of Polymer Matrix Composites Using Indentation Stress-Strain Protocols
Expected completion date Oct 2018
Estimated size (number of pages)
75
Requestor Location Alicia Rossi
5079 Paces Station dr
ATLANTA, GA 30339
United States
Attn: Alicia Ro ssi
Publisher Tax ID 98-0397604
Total 0.00 USD
Terms and Conditions

INTRODUCTION

1. The publisher for this copyrighted material is Elsevier. By clicking "accept" in connection with completing this licensing transaction, you agree that the following terms and conditions apply to this transaction (along with the Billing and Payment terms and conditions established by Copyright Clearance Center, Inc. ("CCC"), at the time that you opened your Rightslink account and that are available at any time at http://myaccount.copyright.com).

GENERAL TERMS

2. Elsevier hereby grants you permission to reproduce the aforementioned material subject to the terms and conditions indicated.

3. Acknowledgement: If any part of the material to be used (for example, figures) hasappeared in our publication with credit or acknowledgement to another source, permission must also be sought from that source. If such permission is not obtained then that material may not be included in your publication/copies. Suitable acknowledgement to the source must be made, either as a footnote or in a reference list at the end of your publication, as follows:

"Reprinted from Publication title, Vol /edition number, Author(s), Title of article / title of chapter, Pages No., Copyright (Year), with permission from Elsevier [OR APPLICABLE SOCIETY COPYRIGHT OWNER]." Also Lancet special credit - "Reprinted from The Lancet, Vol. number, Author(s), Title of article, Pages No., Copyright (Year), with permission from Elsevier."

4. Reproduction of this material is confined to the purpose and/or media for which permission is hereby given.

5. Altering/Modifying Material: Not Permitted. However, figures and illustrations may be altered/adapted minimally to serve your work. Any other abbreviations, additions, deletions and/or any other alterations shall be made only with prior written authorization of Elsevier Ltd. (Please contact Elsevier at permissions@elsevier.com). No modifications can be made to any Lancet figures/tables and they must be reproduced in full.

6. If the permission fee for the requested use of our material is waived in this instance, please be advised that your future requests for Elsevier materials may attract a fee.

7. Reservation of Rights: Publisher reserves all rights not specifically granted in the combination of (i) the license details provided by you and accepted in the course of this licensing transaction, (ii) these terms and conditions and (iii) CCC's Billing and Payment terms and conditions.

8. License Contingent Upon Payment: While you may exercise the rights licensed immediately upon issuance of the license at the end of the licensing process for the transaction, provided that you have disclosed complete and accurate details of your proposed use, no license is finally effective unless and until full payment is received from you (either by publisher or by CCC) as provided in CCC's Billing and Payment terms and conditions. If full payment is not received on a timely basis, then any license preliminarily granted shall be

deemed automatically revoked and shall be void as if never granted. Further, in the event that you breach any of these terms and conditions or any of CCC's Billing and Payment terms and conditions, the license is automatically revoked and shall be void as if never granted. Use of materials as described in a revoked license, as well as any use of the materials beyond the scope of an unrevoked license, may constitute copyright infringement and publisher reserves the right to take any and all action to protect its copyright in the materials.

9. Warranties: Publisher makes no representations or warranties with respect to the licensed material.

10. Indemnity: You hereby indemnify and agree to hold harmless publisher and CCC, and their respective officers, directors, employees and agents, from and against any and all claims arising out of your use of the licensed material other than as specifically authorized pursuant to this license.

11. No Transfer of License: This license is personal to you and may not be sublicensed, assigned, or transferred by you to any other person without publisher's written permission.

12. No Amendment Except in Writing: This license may not be amended except in a writing signed by both parties (or, in the case of publisher, by CCC on publisher's behalf).

13. Objection to Contrary Terms: Publisher hereby objects to any terms contained in any purchase order, acknowledgment, check endorsement or other writing prepared by you, which terms are inconsistent with these terms and conditions or CCC's Billing and Payment terms and conditions. These terms and conditions, together with CCC's Billing and Payment terms and conditions (which are incorporated herein), comprise the entire agreement between you and publisher (and CCC) concerning this licensing transaction. In the event of
any conflict between your obligations established by these terms and conditions and those established by CCC's Billing and Payment terms and conditions, these terms and conditions shall control.

14. Revocation: Elsevier or Copyright Clearance Center may deny the permissions described in this License at their sole discretion, for any reason or no reason, with a full refund payable to you. Notice of such denial will be made using the contact information provided by you. Failure to receive such notice will not alter or invalidate the denial. In no event will Elsevier or Copyright Clearance Center be responsible or liable for any costs, expenses or damage incurred by you as a result of a denial of your permission request, other than a refund of the
amount(s) paid by you to Elsevier and/or Copyright Clearance Center for denied permissions.

LIMITED LICENSE

The following terms and conditions apply only to specific license types:

15. **Translation**: This permission is granted for non-exclusive world **English** rights only unless your license was granted for translation rights. If you licensed translation rights you may only translate this content into the languages you

requested. A professional translator must perform all translations and reproduce the content word for word preserving the integrity of the article.

16. **Posting licensed content on any Website**: The following terms and conditions apply as follows: Licensing material from an Elsevier journal: All content posted to the web site must maintain the copyright information line on the bottom of each image; A hyper-text must be included to the Homepage of the journal from which you are licensing at http://www.sciencedirect.com/science/journal/xxxxx or the Elsevier homepage for books at http://www.elsevier.com; Central Storage: This license does not include permission for a scanned version of the material to be stored in a central repository such as that provided byHeron/XanEdu.

Licensing material from an Elsevier book: A hyper-text link must be included to the Elsevier homepage at http://www.elsevier.com . All content posted to the web site must maintain the copyright information line on the bottom of each image.

Posting licensed content on Electronic reserve: In addition to the above the following clauses are applicable: The website must be password-protected and made available only to bona fide students registered on a relevant course. This permission is granted for 1 year only.

You may obtain a new license for future website posting.

17. **For journal authors:** the following clauses are applicable in addition to the above:

Preprints:

A preprint is an author's own write-up of research results and analysis, it has not been peer-reviewed, nor has it had any other value added to it by a publisher (such as formatting, copyright, technical enhancement etc.).

Authors can share their preprints anywhere at any time. Preprints should not be added to or enhanced in any way in order to appear more like, or to substitute for, the final versions of articles however authors can update their preprints on arXiv or RePEc with their Accepted Author Manuscript (see below).

If accepted for publication, we encourage authors to link from the preprint to their formal publication via its DOI. Millions of researchers have access to the formal publications on ScienceDirect, and so links will help users to find, access, cite and use the best available version. Please note that Cell Press, The Lancet and some society-owned have different preprint policies. Information on these policies is available on the journal homepage.

Accepted Author Manuscripts: An accepted author manuscript is the manuscript of an article that has been accepted for publication and which typically includes author-incorporated changes suggested during submission, peer review and editor-author communications.

Authors can share their accepted author manuscript:

Immediately via their non-commercial person homepage or blog

by updating a preprint in arXiv or RePEc with the accepted manuscript via their research institute or institutional repository for internal institutional uses or as part of an invitation-only research collaboration work-group directly by providing copies to their students or to research collaborators for their personal use for private

scholarly sharing as part of an invitation-only work group on commercial sites with which Elsevier has an agreement. After the embargo period via non-commercial hosting platforms such as their institutional repository via commercial sites with which Elsevier has an agreement.
In all cases accepted manuscripts should:
link to the formal publication via its DOI bear a CC-BY-NC-ND license - this is easy to do if aggregated with other manuscripts, for example in a repository or other site, be shared in alignment with our hosting policy not be added to or enhanced in any way to appear more like, or to substitute for, the published journal article.
Published journal article (JPA): A published journal article (PJA) is the definitive final record of published research that appears or will appear in the journal and embodies all value-adding publishing activities including peer review co-ordination, copy-editing, formatting, (if relevant) pagination and online enrichment.
Policies for sharing publishing journal articles differ for subscription and gold open access articles:
Subscription Articles: If you are an author, please share a link to your article rather than the full-text. Millions of researchers have access to the formal publications on ScienceDirect, and so links will help your users to find, access, cite, and use the best available version.
Theses and dissertations which contain embedded PJAs as part of the formal submission can be posted publicly by the awarding institution with DOI links back to the formal publications on ScienceDirect.
If you are affiliated with a library that subscribes to ScienceDirect you have additional private sharing rights for others' research accessed under that agreement. This includes use for classroom teaching and internal training at the institution (including use in course packs and courseware programs), and inclusion of the article for grant funding purposes.
Gold Open Access Articles: May be shared according to the author-selected end-user license and should contain a CrossMark logo, the end user license, and a DOI link to the formal publication on ScienceDirect. Please refer to Elsevier's posting policy for further information.
18. **For book authors** the following clauses are applicable in addition to the above: Authors are permitted to place a brief summary of their work online only. You are not allowed to download and post the published electronic version of your chapter, nor may you scan the printed edition to create an electronic version. **Posting to a repository:** Authors are permitted to post a summary of their chapter only in their institution's repository.
19. **Thesis/Dissertation**: If your license is for use in a thesis/dissertation your thesis may be submitted to your institution in either print or electronic form. Should your thesis be published commercially, please reapply for permission. These requirements include permission for the Library and Archives of Canada to supply single copies, on demand, of
the complete thesis and include permission for Proquest/UMI to supply single copies, on demand, of the complete thesis. Should your thesis be published

REFERENCES

1. Stewart, R., *Lightweighting the automotive market.* Reinforced plastics, 2009. **53**(2): p. 14-21.

2. Sloan, J. *Making of the BMW i3*. 2014 August 16, 2018]; Available from: https://www.compositesworld.com/blog/post/the-making-of-the-bmw-i3.

3. Brown, S., *Carbon Fiber, Light and Strong, Arrives Where It's Most Needed*, in *The New York Times*. 2013. p. AU2.

4. *Boeing 787 Dreamliner : Aviation: Benefits Beyond Borders*. Value to the economy : Aviation: Benefits Beyond Borders August 16 2018]; Available from: https://aviationbenefits.org/case-studies/boeing-787-dreamliner/.

5. Brosius, D. *Boeing 787 Update*. 2007 August 16, 2018]; Available from: https://www.compositesworld.com/articles/boeing-787-update.

6. Soutis, C., *Fibre reinforced composites in aircraft construction.* Progress in Aerospace Sciences, 2005. **41**(2): p. 143-151.

7. Mallick, P.K., *Materials, design and manufacturing for lightweight vehicles*. 2010: Elsevier.

8. Ghaffaar, M.A., A.A. Mazen, and N.A. El-Mahallawy, *Application of the Rule of Mixtures and Halpin-Tsai Equations to Woven Fabric Reinforced Epoxy Composites*. 2006. p. 227-236.

9. Barham, P.J. and R.G.C. Arridge, *A fiber composite model of highly oriented polyethylene.* Journal of Polymer Science: Polymer Physics Edition, 1977. **15**(7): p. 1177-1188.

10. Clyne, T.W., *A simple development of the shear lag theory appropriate for composites with a relatively small modulus mismatch.* Materials Science and Engineering: A, 1989. **122**(2): p. 183-192.

11. Nettles, A.T., *Basic Mechanics of Laminated Composite Plates.* NASA Reference Publication 1351, 1994.

12. Mortazavi, B., et al., *Modeling of two-phase random composite materials by finite element, Mori–Tanaka and strong contrast methods.* Composites Part B: Engineering, 2013. **45**(1): p. 1117-1125.

13. Mortazavi, B., J. Bardon, and S. Ahzi, *Interphase effect on the elastic and thermal conductivity response of polymer nanocomposite materials: 3D finite element study.* Computational Materials Science, 2013. **69**: p. 100-106.

14. Kamiński, M. and M. Kleiber, *Perturbation based stochastic finite element method for homogenization of two-phase elastic composites.* Computers and Structures, 2000. **78**(6): p. 811-826.

15. Rakesh, P.K., et al., *Delamination in fiber reinforced plastics: A finite element approach.* Scientific research, 2011. **2011**(May): p. 549-554.

16. Maligno, A.R., N.a. Warrior, and a.C. Long, *Finite element investigations on the microstructure of fibre-reinforced composites.* Express Polymer Letters, 2008. **2**(9): p. 665-676.

17. Mishnaevsky, L.L., *Automatic voxel-based generation of 3D microstructural FE models and its application to the damage analysis of composites.* Materials Science and Engineering A, 2005. **407**(1-2): p. 11-23.

18. Lee, S.H., et al., *Evaluation of interphase properties in a cellulose fiber-reinforced polypropylene composite by nanoindentation and finite element analysis.* Composites Part a-Applied Science and Manufacturing, 2007. **38**(6): p. 1517-1524.

19. Reid, A.C.E., et al., *Image-based finite element mesh construction for material microstructures.* Computational Materials Science, 2008. **43**(4): p. 989-999.

20. Cannillo, V., et al., *Investigation of the mechanical properties of Mo-reinforced glass-matrix composites.* Journal of Non-Crystalline Solids, 2004. **344**(1): p. 88-93.

21. Kalidindi, S.R. and E. Franco, *Numerical evaluation of isostrain and weighted-average models for elastic moduli of three-dimensional composites.* Composites Science and Technology, 1997. **57**(3): p. 293-305.

22. Kalidindi, S.R. and A. Abusafieh, *Longitudinal and transverse moduli and strengths of low angle 3-D braided composites.* Journal of Composite Materials, 1996. **30**(8): p. 885-905.

23. Engelstad, S.P., Action, J.E., Clay, S.B., Holzwarth, R.C., Robbins, D., Dalgarno, R. , *Assessment of Composite Damage Growth Tools for Aircraft Structure Part I.* 2014.

24. Stephen, P. and C. Stephen. *Assessment of Composite Damage Growth Tools for Aircraft Structure Part II*. 2016. 57th AIAA/ASCE/AHS/ASC Structures, Structural Dynamics, and Materials Conference.

25. *Standard Test Method for Tensile Properties of Single Textile Fibers*.

26. *Fiber, Matrix, and Interface Properties*. 1996, West Conshohocken, PA: ASTM International.

27. *Standard Test Method for Tensile Properties of Polymer Matrix Composite Materials*. 2014, ASTM International.

28. *Standard Test Method for Compressive Properties of Polymer Matrix Composite Materials with Unsupported Gage Section by Shear Loading*.

29. *Standard Test Method for Flexural Properties of Polymer Matrix Composite Materials*.

30. *Standard Test Method for Determination of the Mode II Interlaminar Fracture Toughness of Unidirectional Fiber-Reinforced Polymer Matrix Composites*.

31. Oliver, W.C. and G.M. Pharr, *Measurement of hardness and elastic modulus by instrumented indentation: Advances in understanding and refinements to methodology.* Journal of Materials Research, 2011. **19**(1): p. 3-20.

32. Desaeger, M. and I. Verpoest, *On the use of the micro-indentation test technique to measure the interfacial shear strength of fibre-reinforced polymer composites.* Composites Science and Technology, 1993. **48**(1): p. 215-226.

33. Desaeger, M. and I. Verpoest, *On the Use of the Micro-Indentation Test Technique to Measure the Interfacial Shear-Strength of Fiber-Reinforced Polymer Composites.* Composites Science and Technology, 1993. **48**(1-4): p. 215-226.

34. Kharrat, M. and A. Chateauminois, *On the interfacial behaviour of a glass/epoxy composite during a micro-indentation test: Assessment of interfacial shear strength using reduced indentation curves.* Composites Part a-Applied Science and Manufacturing, 1997. **28**(1): p. 39-46.

35. Herrera-Franco, P.J. and L.T. Drzal, *Comparison of methods for the measurement of fibre/matrix adhesion in composites.* Composites, 1992. **23**(1): p. 2-27.

36. Hodzic, A., et al., *Application of nano-indentation, nano-scratch and single fibre tests in investigation of interphases in composite materials.* Micron, 2001. **32**(8): p. 765-775.

37. Hodzic, A., et al., *The effects of water aging on the interphase region and interlaminar fracture toughness in polymer-glass composites.* Composites Science and Technology, 2004. **64**(13-14): p. 2185-2195.

38. Hodzic, A., J.K. Kim, and Z.H. Stachurski, *Nano-indentation and nano-scratch of polymer/glass interfaces. II: model of interphases in water aged composite materials.* Polymer, 2001. **42**(13): p. 5701-5710.

39. Hodzic, A., Z.H. Stachurski, and J.K. Kim, *Nano-indentation of polymer-glass interfaces Part I. Experimental and mechanical analysis.* Polymer, 2000. **41**(18): p. 6895-6905.

40. Wang, H.Y., et al., *Combined effects of silica filler and its interface in epoxy resin.* Acta Materialia, 2002. **50**(17): p. 4369-4377.

41. Young, T.J., et al., *Observations on interphase characterisation in polymer composites by nano-scale indentation using AFM and FEA.* Composites Part a-Applied Science and Manufacturing, 2013. **50**: p. 39-43.

42. Mallikarjunachari, G. and P. Ghosh, *Analysis of strength and response of polymer nano thin film interfaces applying nanoindentation and nanoscratch techniques.* Polymer, 2016. **90**: p. 53-66.

43. Oliver, W.C. and G.M. Pharr, *Measurement of hardness and elastic modulus by instrumented indentation: Advances in understanding and refinements to methodology.* Journal of Materials Research, 2004. **19**(1): p. 3-20.

44. Tabor, D., *The Hardness of Metals*. 1951: Oxford University Press.

45. Field, J.S. and M.V. Swain, *A Simple Predictive Model for Spherical Indentation.* Journal of Materials Research, 1993. **8**(2): p. 297-306.

46. Field, J.S. and M.V. Swain, *Determining the mechanical properties of small volumes of material from submicrometer spherical indentations.* Journal of Materials Research, 1995. **10**(1): p. 101-112.

47. Herbert, E.G., et al., *On the measurement of stress-strain curves by spherical indentation.* Thin Solid Films, 2001. **398-399**: p. 331-335.

48. Basu, S., A. Moseson, and M.W. Barsoum, *On the determination of spherical nanoindentation stress–strain curves.* Journal of Materials Research, 2006. **21**(10): p. 2628-2637.

49. Kalidindi, S.R. and S. Pathak, *Determination of the effective zero-point and the extraction of spherical nanoindentation stress-strain curves.* Acta Materialia, 2008. **56**(14): p. 3523-3532.

50. Patel, D.K. and S.R. Kalidindi, *Correlation of spherical nanoindentation stress-strain curves to simple compression stress-strain curves for elastic-plastic isotropic materials using finite element models.* Acta Materialia, 2016. **112**: p. 295-302.

51. Patel, D.K. and S.R. Kalidindi, *Estimating the slip resistance from spherical nanoindentation and orientation measurements in polycrystalline samples of cubic metals.* International Journal of Plasticity, 2017. **92**: p. 19-30.

52. Weaver, J.S. and S.R. Kalidindi, *Mechanical characterization of Ti-6Al-4V titanium alloy at multiple length scales using spherical indentation stress-strain measurements.* Materials and Design, 2016. **111**: p. 463-472.

53. Khosravani, A., A. Cecen, and S.R. Kalidindi, *Development of High Throughput Assays for Establishing Process-Structure-Property Linkages in Multiphase Polycrystalline Metals: Application to Dual-Phase Steels.* Acta Materialia, 2016. **submitted**.

54. Vachhani, S.J., R.D. Doherty, and S.R. Kalidindi, *Studies of grain boundary regions in deformed polycrystalline aluminum using spherical nanoindentation.* International Journal of Plasticity, 2016. **81**: p. 87-101.

55. Weaver, J.S., et al., *High throughput exploration of process-property linkages in Al-6061 using instrumented spherical microindentation and microstructurally graded samples.* Integrating Materials and Manufacturing Innovation, 2016. **5**(1): p. 10.

56. Pathak, S., S.R. Kalidindi, and N.A. Mara, *Investigations of orientation and length scale effects on micromechanical responses in polycrystalline zirconium using spherical nanoindentation.* Scripta Materialia, 2016. **113**: p. 241-245.

57. Pathak, S. and S.R. Kalidindi, *Spherical nanoindentation stress-strain curves.* Materials Science & Engineering R-Reports, 2015. **91**: p. 1-36.

58. Pathak, S., et al., *Measuring the dynamic mechanical response of hydrated mouse bone by nanoindentation.* Journal of the Mechanical Behavior of Biomedical Materials, 2011. **4**: p. 34-43.

59. Pathak, S., et al., *Importance of surface preparation on the nano-indentation stress-strain curves measured in metals.* Journal of Materials Research, 2009. **24**(3): p. 1142-1155.

60. Pathak, S., et al., *Viscoelasticity and high buckling stress of dense carbon nanotube brushes.* Carbon, 2009. **47**(8): p. 1969-1976.

61. Hertz, H., *Miscellaneous Papers*. 1896, New York: MacMillan and Co., Ltd.

62. Pathak, S., J. Shaffer, and S.R. Kalidindi, *Determination of an effective zero-point and extraction of indentation stress-strain curves without the continuous stiffness measurement signal.* Scripta Materialia, 2009. **60**(6): p. 439-442.

63. Vachhani, S.J., R.D. Doherty, and S.R. Kalidindi, *Effect of the continuous stiffness measurement on the mechanical properties extracted using spherical nanoindentation.* Acta Materialia, 2013. **61**(10): p. 3744-3751.

64. Donohue, B.R., A. Ambrus, and S.R. Kalidindi, *Critical evaluation of the indentation data analyses methods for the extraction of isotropic uniaxial mechanical properties using finite element models.* Acta Materialia, 2012. **60**: p. 3943–3952.

65. Ng, Y.-C., *Deriving Composite Lamina Properties from Laminate Properties Using Classical Lamination Theory and Failure Criteria.* Journal of Composite Materials, 2016. **39**(14): p. 1295-1306.

66. Flaggs, D.K., M, *Experimental Determination of the In Situ Transverse Lamina Strength in Graphite/Epoxy Laminates.* Journal of Composite Materials, 1982. **16**: p. 103-116.

67. Huang, Z.M., *Simulation of the mechanical properties of fibrous composites by the bridging micromechanics model.* Composites Part a-Applied Science and Manufacturing, 2001. **32**(2): p. 143-172.

68. Hardiman, M., T.J. Vaughan, and C.T. McCarthy, *A review of key developments and pertinent issues in nanoindentation testing of fibre reinforced plastic microstructures.* Composite Structures, 2017. **180**: p. 782-798.

69. Gregory, J. and S. Spearing, *Nanoindentation of neat and polymers in polymer?matrix composites.* Composites Science and Technology, 2005. **65**(3-4): p. 595-607.

70. Pharr, G.M. and W.C. Oliver, *Measurement of Thin Film Mechanical Properties Using Nanoindentation.* MRS Bulletin, 2013. **17**(7): p. 28-33.

71. Pathak, S., et al., *Importance of surface preparation on the nano-indentation stress-strain curves measured in metals.* Journal of Materials Research, 2009. **24**(03): p. 1142-1155.

72. Weaver, J.S. and S.R. Kalidindi, *Mechanical characterization of Ti-6Al-4V titanium alloy at multiple length scales using spherical indentation stress-strain measurements.* Materials & Design, 2016. **111**: p. 463-472.

73. Wei, G. and P.X. Ma, *Structure and properties of nano-hydroxyapatite/polymer composite scaffolds for bone tissue engineering.* Biomaterials, 2004. **25**(19): p. 4749-57.

74. Pathak, S., et al., *Measuring the dynamic mechanical response of hydrated mouse bone by nanoindentation.* Journal of the mechanical behavior of biomedical materials, 2011. **4**(1): p. 34-43.

75. Abba, M.T., *Spherical Nanoindentation Protocols for Extracting Microscale Mechanical Properties in Viscoelastic Materials.* 2015(December).

76. Clay, S.B. and P.M. Knoth, *Experimental results of fatigue testing for calibration and validation of composite progressive damage analysis methods.* Journal of Composite Materials, 2016.

77. Clay, S.B. and P.M. Knoth, *Experimental results of quasi-static testing for calibration and validation of composite progressive damage analysis methods.* Journal of Composite Materials, 2016. **51**(10): p. 1333-1353.

78. Patel, D. and S. Kalidindi, *Estimating the slip resistance from spherical nanoindentation and orientation measurements in polycrystalline samples of cubic metals.* International Journal of Plasticity, 2017. **92**: p. 19.

79. Patel, D.K., H.F. Al-Harbi, and S.R. Kalidindi, *Extracting single-crystal elastic constants from polycrystalline samples using spherical nanoindentation and orientation measurements.* Acta Materialia, 2014. **79**: p. 108-116.

80. Priddy, M.W., *Exploration of forward and inverse protocols for property optimization of Ti-6Al-4V*, D.L. McDowell, et al., Editors. 2016, Georgia Institute of Technology.

81. Bhattacharya, A.K. and W.D. Nix, *Finite element simulation of indentation experiments.* International Journal of Solids and Structures, 1988. **24**(9): p. 881-891.

82. Chamis, C.C., *Mechanics of Composite-Materials - Past, Present, and Future.* Journal of Composites Technology & Research, 1989. **11**(1): p. 3-14.

83. Bhuiyan, M.A., et al., *Tensile modulus of carbon nanotube/polypropylene composites - A computational study based on experimental characterization.* Computational Materials Science, 2011. **50**(8): p. 2347-2353.

84. Abba, M.T., *Spherical Nanoindentation Protocols for Extracting Microscale Mechanical Properties in Viscoelastic Materials Spherical Nanoindentation Protocols for Extracting Microscale Mechanical Properties in.* 2015(December).

85. Swadener, J.G., George, E. P., Pharr, G.M., *The correlation of the indentation size effect measured with indenters of various shapes.* Journal of the Mechanics and Physics of Solids, 2002. **Volume 50**(4): p. 681-694.

86. Milton, G.W., *The Theory of Composites.* Cambridge monographs on applied and computational mathematics., 2002.

87. Hallal, A., R. Younes, and F. Fardoun, *Review and comparative study of analytical modeling for the elastic properties of textile composites.* Composites Part B: Engineering, 2013. **50**: p. 22-31.

88. Del Vecchio, C., et al., *Analytical model and design approach for FRP strengthening of non-conforming RC corner beam–column joints.* Engineering Structures, 2015. **87**: p. 8-20.

89. Mortazavian, S. and A. Fatemi, *Effects of fiber orientation and anisotropy on tensile strength and elastic modulus of short fiber reinforced polymer composites.* Composites Part B: Engineering, 2015. **72**: p. 116-129.

90. Zeng, D., et al. *Modeling of Long Fiber Reinforced Plastics*.

91. Buck, F., et al., *Two-scale structural mechanical modeling of long fiber reinforced thermoplastics.* Composites Science and Technology, 2015. **117**: p. 159-167.

92. Vanaerschot, A., et al., *Stochastic multi-scale modelling of textile composites based on internal geometry variability.* Computers and Structures, 2013. **122**: p. 55-64.

93. Phelps, J.H., et al., *A model for fiber length attrition in injection-molded long-fiber composites.* Composites Part A: Applied Science and Manufacturing, 2013. **51**: p. 11-21.

94. Gupta, A., et al., *Structure–property linkages using a data science approach: Application to a non-metallic inclusion/steel composite system.* Acta Materialia, 2015. **91**: p. 239-254.

95. Çeçen, A., et al., *A data-driven approach to establishing microstructure–property relationships in porous transport layers of polymer electrolyte fuel cells.* Journal of Power Sources, 2014. **245**: p. 144-153.

96. Wheeler, D., et al., *Materials Knowledge Systems in Python — PyMKS*. 2014.

97. Cecen, A., T. Fast, and S.R. Kalidindi, *Versatile algorithms for the computation of 2-point spatial correlations in quantifying material structure.* Integrating Materials and Manufacturing Innovation, 2016. **5**(1): p. 1-1.

98. Niezgoda, S., A. Kanjarla, and S. Kalidindi, *Novel microstructure quantification framework for databasing, visualization, and analysis of microstructure data.* Integrating Materials and Manufacturing Innovation, 2013. **2**(1): p. 1-27.

99. Niezgoda, S.R., Y.C. Yabansu, and S.R. Kalidindi, *Understanding and visualizing microstructure and microstructure variance as a stochastic process.* Acta Materialia, 2011. **59**(16): p. 6387-6400.